



TECHNISCHE
UNIVERSITÄT
WIEN



DIPLOMARBEIT

Development and Optimization of a Carbon-Nanotube Based Electron Gun

zur Erlangung des akademischen Grades

Diplom-Ingenieurin

im Rahmen des Studiums

Biomedical Engineering

eingereicht von

Elisabeth-Sena Welker, BSc

ausgeführt am

CERN, Esplanade des Particules 1/1211, Genf, Schweiz

Betreuung

Privatdoz. Dipl.-Ing. Dr.techn. Michael Benedikt (Atominstitut, TU Wien)

Gerard Tranquille (CERN)

Ass.Prof.in Dipl.-Ing.in Dr.in techn. Karin Poljanc (Atominstitut, TU Wien)

Wien, 03.02.2025

(Unterschrift Verfasserin)

(Unterschrift Betreuer)



Die approbierte gedruckte Originalversion dieser Diplomarbeit ist an der TU Wien Bibliothek verfügbar
The approved original version of this thesis is available in print at TU Wien Bibliothek.

Affidavit

I declare in lieu of oath, that I wrote this thesis and performed the associated research myself, using only literature cited in this volume. If text passages from sources are used literally, they are marked as such.

I confirm that this work is original and has not been submitted elsewhere for any examination, nor is it currently under consideration for a thesis elsewhere. I acknowledge that the submitted work will be checked electronically-technically using suitable and state-of-the-art means (plagiarism detection software). On the one hand, this ensures that the submitted work was prepared according to the high-quality standards within the applicable rules to ensure good scientific practice "Code of Conduct" at the TU Wien. On the other hand, a comparison with other student theses avoids violations of my personal copyright.

Date

Signature



Die approbierte gedruckte Originalversion dieser Diplomarbeit ist an der TU Wien Bibliothek verfügbar
The approved original version of this thesis is available in print at TU Wien Bibliothek.

Eidesstattliche Erklärung

Ich erkläre an Eides statt, dass die vorliegende Arbeit nach den anerkannten Grundsätzen für wissenschaftliche Abhandlungen von mir selbstständig erstellt wurde. Alle verwendeten Hilfsmittel, insbesondere die zugrunde gelegte Literatur, sind in dieser Arbeit genannt und aufgelistet. Die aus den Quellen wörtlich entnommenen Stellen, sind als solche kenntlich gemacht. Das Thema dieser Arbeit wurde von mir bisher weder im In- noch Ausland einer Beurteilerin/einem Beurteiler zur Begutachtung in irgendeiner Form als Prüfungsarbeit vorgelegt. Diese Arbeit stimmt mit der von den Begutachterinnen/Begutachtern beurteilten Arbeit überein.

Datum

Unterschrift



Die approbierte gedruckte Originalversion dieser Diplomarbeit ist an der TU Wien Bibliothek verfügbar
The approved original version of this thesis is available in print at TU Wien Bibliothek.

Abstract

Field emission (FE)-based cathodes have become a promising alternative to thermionic sources, which suffer from high transverse energy spread and high power consumption. Here, a carbon-nanotube (CNT)-based electron gun was studied as a potential replacement for the thermionic gun currently used in the electron cooler of the Extra Low ENergy Antiproton (ELENA) decelerator at CERN. Earlier investigations on a cold cathode test bench (CCTB1) found that honeycomb-patterned, vertically aligned CNT (VACNT) arrays ($1 \times 1 \text{ cm}^2$ surface area) could function as a feasible FE source, leading to the proposal of a dual-gridded electron gun prototype.

This study focuses on three core objectives: (1) fabricate and characterize larger (up to $4 \times 4 \text{ cm}^2$) patterned VACNT samples for use in the electron gun; (2) modify CCTB1 to include a beam transport and diagnostic system to test the prototype's proof of concept; (3) compare experimental findings with previously conducted simulations to anticipate beam behavior.

Fowler-Nordheim analysis confirmed field-emission-based operation in all samples, with larger samples showing better FE performance. However, the current density was significantly lower than expected. An electron beam was successfully generated from a large sample implemented the improved prototype, but it exhibited greater divergence and a larger radius than simulations predicted. Overall, the results confirm that VACNT-based cold cathodes can serve as viable source in a gridded electron gun configuration, warranting future research and development efforts.

Kurzfassung

Feldemissions-(FE)-basierte Kathoden haben sich zu einer vielversprechenden Alternative zu thermionischen Quellen entwickelt, da letztere mit einer hohen transversalen Energiebreite und hohem Stromverbrauch behaftet sind. In dieser Arbeit wurde eine auf Kohlenstoffnanoröhren (CNT) basierende Elektronenkanone als potenzieller Ersatz für die derzeit im Elektronenkühler des Extra Low ENergy Antiproton (ELENA)-Decelerators am CERN verwendete thermionische Kanone untersucht. Frühere Studien an einer so genannten Cold Cathode Test Bench (CCTB1) zeigten, dass wabenförmig angeordnete, vertikal ausgerichtete CNTs (VACNT) mit einer Fläche $1 \times 1 \text{ cm}^2$ eine geeignete FE-Quelle darstellen können. Darauf aufbauend wurde ein Prototyp für eine zweifach gegitterte Elektronenkanone vorgeschlagen.

Diese Untersuchung hatte drei Hauptziele: Erstens wurde die Fertigung und Charakterisierung größerer (bis zu $4 \times 4 \text{ cm}^2$) VACNT-Proben für den Einsatz in der Elektronenkanone durchgeführt. Zweitens wurde die CCTB1 modifiziert, um ein Strahltransportsystem und entsprechende Diagnoseinstrumente zu integrieren und so das Proof-of-Concept des Prototyps zu testen. Drittens wurden die experimentellen Ergebnisse mit bereits durchgeführten Simulationen abgeglichen, um das Strahlverhalten vorhersagen zu können.

Die Fowler-Nordheim-Analyse bestätigte, dass für alle Proben Ströme basierend auf Feldemission gemessen wurden, wobei größere Proben eine bessere FE-Leistung aufwiesen. Allerdings fiel die Stromdichte deutlich geringer aus als erwartet. Mit einer großen Probe, die in den verbesserten Prototyp integriert wurde, konnte erfolgreich ein Elektronenstrahl erzeugt werden, jedoch zeigte dieser eine stärkere Divergenz und einen größeren Radius als die Simulationen vorhergesagt hatten. Insgesamt bestätigen die Resultate, dass VACNT-basierte Kathoden eine brauchbare Quelle in einer gegitterten Elektronenkanone darstellen können und rechtfertigen weitere Forschungs- und Entwicklungsarbeiten zu dem Thema.

Contents

1	Introduction	1
2	Background	3
2.1	CERN	3
2.1.1	AD & ELENA	5
2.2	Basics of Beam Physics	5
2.2.1	Phase Space	6
2.2.2	Emittance	6
2.2.3	Longitudinal Momentum Spread	8
2.3	Electron Cooling Theory	8
2.3.1	Motivation for Electron Cooling in ELENA	8
2.3.2	Implementation of Electron Cooling	10
2.3.3	Electron Cooling Time	11
2.3.4	Cooler Magnet System	12
2.4	Electron Emission Theory	12
2.4.1	Electron Sources	13
2.4.2	Fowler-Nordheim Theory	14
2.4.3	Generalized FN-equation	16
2.5	Carbon-Nanotubes (CNTs)	17
2.5.1	CNT based Field Emission	18
2.5.2	VACNTs	19
2.5.3	Factors affecting FE efficiency in VACNTs	20
2.6	Electron Guns	21
2.6.1	Basic theory of Electron Guns	21
2.6.2	Gun design considerations for Electron Cooling	22
3	Experimental Study	25
3.1	The Electron Gun	25
3.1.1	Components of the Electron Gun	25
3.1.2	Challenges and Optimization of the Gun Design	25
3.1.3	Einzel Lens System	27
3.1.4	CNT samples	28
3.2	Testbench Set-up	30
3.2.1	CCTB2	30
3.2.2	CCTB1 flange	30
3.2.3	Data acquisition and analysis	31
3.3	Microscopic analysis	32
4	Simulation Study	33
4.1	Simulation Overview	33
4.1.1	Simulation Strategy	33
4.2	CST Simulations (Stage 1)	34

4.2.1	Simulation Configuration	35
4.2.2	Parameter Monitoring and Post-Processing for COMSOL	35
4.3	COMSOL Simulations (Stage 2)	36
4.3.1	Simulation Configuration	37
5	Simulation Results	39
5.1	Stage 1	39
5.1.1	Beam Characteristics	39
5.1.2	Electric Field and Particle Trajectories	39
5.1.3	Maximal Orbital Angle	39
5.2	Stage 2	41
5.2.1	Electric Field and Particle Trajectories	41
5.2.2	Beam Profile	43
6	Experimental Results	47
6.1	Field Emission Performance CCTB1	47
6.1.1	Conditioning, Lifetime and Long-term Stability of VACNTs	47
6.1.2	Characterization and Field Emission Properties	47
6.1.3	Fowler–Nordheim plot analysis	49
6.2	Electron Beam Profile CCTB2	50
7	Discussion	53
7.1	Simulation	53
7.1.1	Stage 1	53
7.1.2	Stage 2	54
7.2	Experimental Data	55
7.2.1	Field Emission Performance CCTB1	55
7.2.2	Electron Beam Profile CCTB2	57
8	Potential Applications in Medicine	59
	Bibliography	63

List of Figures

2.1	Overview of CERN's accelerator complex, various types of particles are distinguished with arrowheads of distinct colors [3] . . .	4
2.2	ELENA topview, primary components: dipole magnets in blue, quadrupole magnets in orange/red and the electron cooler towers in lighter blue [3]	4
2.3	Illustration of a typical ELENA antiproton cycle. The solid black line represents the circulating beam; periods highlighted in red and blue indicate operation of RF cavities and electron cooling system, respectively. [11]	5
2.4	Phase space ellipse representation (adapted from [17])	7
2.5	Schematic diagram of the effect of beam cooling: (a) on the beam size, and (b) on the momentum spread [18]	9
2.6	Mechanical drawing of the ELENA Electron Cooler, the particle trajectories are illustrated with arrows; adapted from [20]	10
2.7	Three main mechanisms of electron emission: (a) Thermionic emission via heating, (b) Photoelectric emission by photon-electron interaction and (c) Field emission due to an applied electric field E . [13]	13
2.8	Field emission potential diagram at the metal-vacuum interface. The bending of the surface barrier is due to the combined effect of the applied electric field and the image potential, resulting in the effective potential $V(z)$. On the left, $N(E)$ illustrates the fluctuations in electron density within the emitter, while the current density $J(E)$ is a function of energy E of the tunneled electron and is represented on the right side [30]	15
2.9	Schematics: (a) A graphene sheet rolled up to form a single CNT, (b) Vertically aligned CNTs on a substrate.	17
2.10	Example of a Seppen-Katamuki plot with interpretation of FN characteristics [38]	19
2.11	Spatial distribution of the electric potential near CNTs for various inter-tube distances. (a) Single CNT, (b) Three widely spaced CNTs and (c) Three moderately spaced CNTs. The closer the nanotubes, the lower the electric field enhancement factor [44].	20
2.12	Emission stability test in switching mode for a honeycomb-like array with an applied electric field of $E = 2 \text{ V}/\text{m}$. The test was performed for around 14 hours in switching mode, followed by DC mode to compare stability [9].	23
3.1	Optical microscopy of the grid; showing a corner of the meshed area, with the grid comprising of $15 \mu\text{m}$ square holes with $3 \mu\text{m}$ walls	26

3.2	Schematic illustration of the CNT-based electron gun working principle: The sample holder contains the CNT sample grown on a Si-wafer. Three voltages are applied: U_{CNT} , U_{grid1} and U_{grid2} to enable tunneling. The emitted electrons pass through grid 1 and grid 2, which are placed 1.4 mm and 19.75 mm above the CNT sample, respectively. The arrows indicate the direction of the emitted electrons.	26
3.3	(a) Cross-sectional view of the mechanical model of the CNT-based electron gun, showing the arrangement of the Einzel lenses, emitter region and rod structure, (b) Exploded view of the emitter region, including the Vespel® mask, CNT sample, metal screw supplying high voltage, PEEK screws, two spacers and focusing electrode.	27
3.4	SEM images by George Machado Jr. (INL) showing (a) the height of the VACNTs from a tilted perspective, (b) the VACNTs arranged in a hexagonal pattern (10 μm side length, 2 μm gap). . .	28
3.5	Final electron gun setup used in the experiments.	29
3.6	Inlays made of Vespel® (1 cm^2 , 2 cm^2 , 3 cm^2) for different sample sizes. The top-right plate is for reference.	30
3.7	Cold-Cathode-Test-Bench 2: ① Vacuum tank with gun assembly ② Pfeiffer Vacuum Dual Gauge ③ PHOTONICS Ion Beam Profiler ④ HM6012 Multimeter ⑤ ISEG HV Power Supplies	31
3.8	(a) Schematic of the CCTB1 sample holder stack, showing the key components: the anode plate (I_{meas}), insulating mask, CNT sample, steel sample holder and mica plate. A high voltage ($U \sim kV$) is applied across the assembly to enable electron emission from the CNT sample. (b) Top view of the CCTB1 setup, showing one mounted sample and the overall configuration	31
4.1	Illustration of simulation layout	34
5.1	Comparison of the Beam Divergence Angle, Emittance \times and Maximum Transversal Position over the distance along the beam path	40
5.2	Comparison of the Mean Energy and the Transparency over the distance along the beam path	41
5.3	Illustrations showing (a) electric potential distribution, (b) particle trajectories and (c) equipotential lines near the first grid.	42
5.4	Beam trajectory and equipotential surfaces in COMSOL	44
5.5	Beam shapes at detector distance for various applied voltages V_M	45
6.1	Ramp-up and stability measurement for sample $2 \times 2 \text{ cm}^2$ performed on CCTB1.	48
6.2	Current density for different samples sizes	49
6.3	Fowler–Nordheim analysis	51
6.4	Images of the beam spot on the phosphor screen	52
8.1	Schematic image of depth-dose profiles of a photon (red), proton (black) and antiproton beam (blue). The deposited energy is expressed relative to the plateau region. [58]	59

List of Tables

2.1	Electron Cooler Parameters for ELENA during intermediate and ejection cooling plateau [9]	9
3.1	Summary of CNT sample requirements	29
4.1	Comparison of simulation parameters for different scales	36
4.2	Parameters used in the COMSOL simulation. The value of $\bar{\sigma}_m$ can be found in subsection 5.1.3.	37
5.1	Maximum Orbital Angle extracted from differently scaled CST simulations	39
5.2	Beam Radius and Area at different middle lens voltages	43
6.1	Turn-on field (E_{on}) and threshold field ($E_{threshold}$) at 0.01 mA/cm ² and 0.1 mA/cm ² for different datasets	47
6.2	Fitting parameters for different datasets.	50

1 Introduction

Electron sources are an important part of many vacuum devices, including electron microscopes, free-electron lasers, medical imaging systems and X-ray sources. Historically, these sources have relied on thermionic cathodes — heated metal filaments that emit electrons [1, 2]. One notable application of electron sources can be found in the Extra Low ENergy Antiproton (ELENA) deceleration system at CERN, where antiprotons are slowed from 5.3 MeV down to 100 keV. ELENA delivers the antiprotons to antimatter experiments for trapping and antihydrogen production. Currently, five experiments (ALPHA, ASACUSA, BASE, AEGIS and GBAR) depend on antiprotons from ELENA [3].

A key component of the deceleration process is electron cooling, where an overlapped monochromatic electron beam reduces the energy spread of the antiproton beam. It has been established that the efficiency of cooling depends on the transverse energy spread of the emitted electrons [4]. Traditionally, these electron beams are generated using thermionic cathodes, however, they present certain limitations. Even though these cathodes offer a long lifetime, their reliance on high temperatures introduces an inherently high thermal energy spread ($T_{\perp} \approx 0.1$ eV). Further drawbacks are a high energy consumption and slow response time [2, 5]. Improving electron cooling by using a “colder” cathode (i.e. one with a lower transverse energy) could overcome these limitations while still fulfilling the ELENA operational requirements [6].

Over the past two decades field emission (FE) has become a promising alternative to thermionic sources. Field emission cathodes only require high electric fields ($\sim 10^7$ V/cm) to induce quantum tunneling of electrons to extract them out of the donor material, eliminating the need of extra heating of the source [7].

Among the materials investigated for field emission cathodes, Carbon Nanotubes (CNTs) have been considered as very promising due to their exceptional properties, such as high aspect ratio, good current stability and relatively low turn-on electric field [8]. Their feasibility as field emitters has been well studied. Previous studies have tested different types of CNT arrays for use in electron guns, including vertically aligned CNT forests grown on predefined patterns on a silicon wafer. Lifetime and stability investigations have demonstrated remarkable performance, with CNT cathodes operating for over 1500 hours and achieving current densities of up to 2 mA cm^{-2} . These results confirm that CNT-based cathodes are viable candidates for the electron cooler in ELENA [9].

Still, there remains a major research gap in determining the optimal field emission characteristics and the practical integration of CNTs in macroscopic devices and a complex accelerator system. Bridging this gap is essential for advancing the development of a more efficient electron gun system.

In previous studies by Galante [9], a diagnostic cold cathode test bench (CCTB1) was developed at CERN and used to measure beam properties of a CNT-based electron emitter. It has been utilized to analyze different types of small CNT

arrays (1 cm × 1 cm). Based on the obtained results, a prototype for a dual-gridded CNT-based electron gun has been proposed. The layout is comprised of the sample holder and the CNT sample, different insulating ceramic spacers, two fine mesh grids, high-voltage feedthroughs and electrostatically focusing Einzel-lenses.

One aim of this thesis is to test and eventually install the prototype on a specifically designed testbench. This will require updating the CCTB to include an ultra-high vacuum tank and the necessary diagnostics for the experiments. Furthermore, the goal is to design and fabricate larger CNT arrays based on the findings of Galante, which indicate that honeycombed patterned arrays exhibit better field emission properties compared to full forests [9]. Another objective is to study the feasibility of using CNTs in ELENA by characterizing the emission properties, current density and stability for different sample sizes.

Charged particle simulations using finite element software are planned to precede the experimental work. The goal is to analyze the electron gun setup, predict the beam at full-scale operation and compare the data to the experimental measurements.

The overall objective of this project is to improve the electron cooling process, leading to less beam loss and a higher quality beam, which in turn enhances antiproton capture efficiencies in antimatter experiments. This could lead to more precise studies in the production and investigation of antihydrogen atoms and contribute to the potential application of antiprotons as a modality in radiation therapy.

This thesis is divided into seven chapters: Chapter 2 provides the foundation of basic concepts in beam physics, electron cooling and field emission. Chapters 3 and 4 summarize the methods used for the experimental and simulation work, while Chapters 5 and 6 present the corresponding results. Chapter 7 discusses the obtained findings, while the last chapter outlines the potential application for medical purposes like cancer treatment.

2 Background

2.1 CERN

The “Conseil Européen pour la Recherche Nucléaire”, or **European Council for Nuclear Research (CERN)** was established in 1954 as a cooperative venture among 12 European countries. Located near Geneva, on the Franco-Swiss border, CERN is dedicated to fostering scientific collaboration and providing insights into the most fundamental questions about the nature of our universe. In its quest for knowledge, CERN has achieved many major scientific milestones, notably the discovery of the W and Z boson (1983), the Top quark (1995) and the Higgs boson (2012).

Equally noteworthy are CERN’s studies of antimatter at low energies and the production and maintenance of anti-hydrogen (one antiproton and one positron). Recently, the **ALPHA-g** experiment published groundbreaking results proving that antimatter particles behave in a way consistent with gravitational attraction to the Earth - similarly to their matter counterparts [3, 10].

Accelerator Complex

CERN encompasses a series of accelerators, that were successively designed and constructed over the years in order to accelerate charged particle beams to different energies. The initial component is the linear accelerator **Linac4**, that produces a H-ion beam with a kinetic energy of 160 MeV (50% the speed of light). Subsequently, a sequence of synchrotrons, namely the **Proton Synchrotron Booster (PSB)**, the **Proton Synchrotron (PS)** and the **Super Proton Synchrotron (SPS)** accelerate the proton beam to 450 GeV. The beam is then injected into the worlds largest and most powerful particle accelerator, the **Large Hadron Collider (LHC)**. The LHC increases the particles energy up to 7 TeV, corresponding to 99.999 999 1% the speed of light.

Two proton beams circulate the LHC in opposing directions and are directed to collide at four interaction points, aligning with the positions of four particle detectors – namely, **ATLAS**, **CMS**, **ALICE** and **LHCb**. While ATLAS and CMS are general purpose detectors, ALICE is dedicated to the physics of heavy ions and LHCb focuses at studying the bottom quark. CERN’s research scope reaches also beyond particle physics, as it hosts many other facilities. These include but are not limited to: neutrino physics (CERN Neutrino Platform), galactic cosmic ray (CLOUD) and medical isotope production (MEDICIS) [3]. The complex network of accelerators and experiments at CERN is depicted in [Figure 2.1](#). The topic of this thesis is dedicated to the low energy antimatter physics with the **Antiproton Decelerator (AD)** and the **Extra Low Energy Antiproton (ELENA)** decelerator (see [Figure 2.2](#)), which will be discussed in the following section.

The CERN accelerator complex Complexe des accélérateurs du CERN

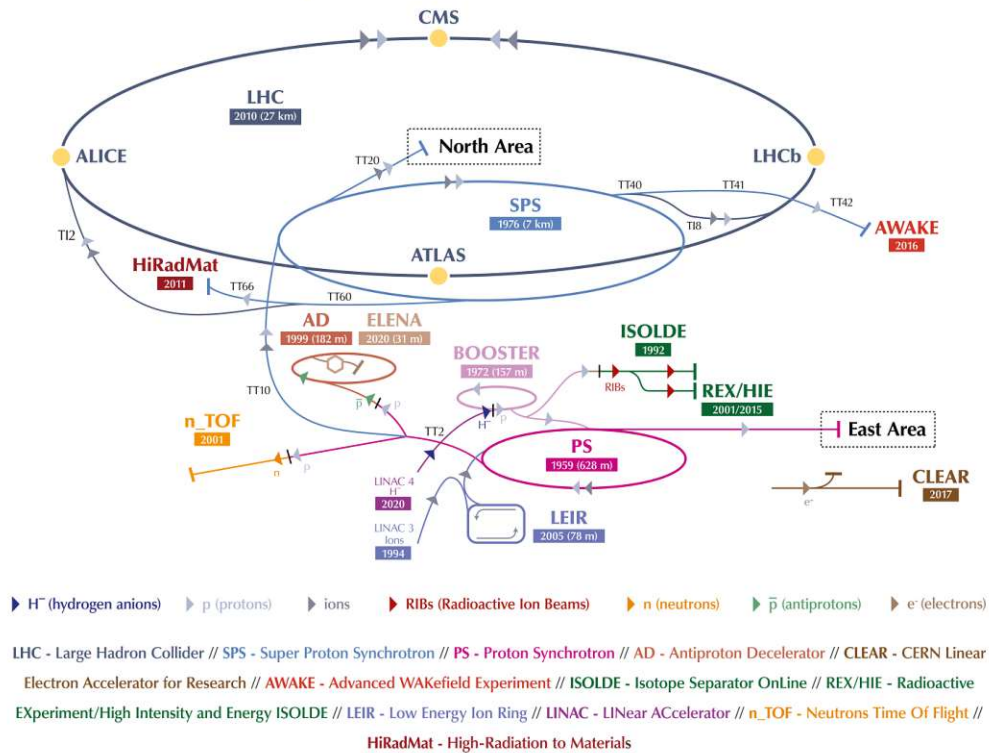


Figure 2.1: Overview of CERN’s accelerator complex, various types of particles are distinguished with arrowheads of distinct colors [3]

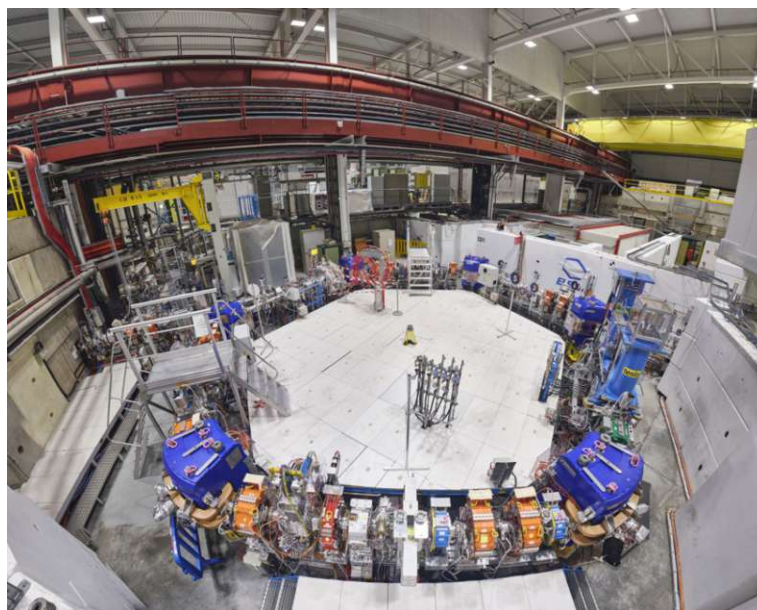


Figure 2.2: ELEN topview, primary components: dipole magnets in blue, quadrupole magnets in orange/red and the electron cooler towers in lighter blue [3]

2.1.1 AD & ELENA

To produce antimatter, protons are obtained by the PS at 30 GeV and collided against an iridium target. These collisions generate numerous secondary particles, including antiprotons, which are selected by employing a magnetic field. However, they possess too much energy for effective antimatter production and are subsequently sent into the AD. The AD's purpose is to decelerate the particles down to 10% of the speed of light and deliver the beam to ELENA. ELENA is a small accelerator with a 30-meter circumference, that then further reduces the energy of antiprotons by a factor of 50, from 5.3 MeV to a mere 100 keV. A typical antiproton deceleration cycle is depicted in Figure 2.3.

Following the injection of a single bunch into a **Radio Frequency** (RF) bucket (at 100 MeV/c), the beam undergoes deceleration to 35 MeV/c. At this point, the beam is de-bunched and electron cooling is switched on. Following the re-bunching process, the beam is decelerated to the extraction momentum of 13.7 MeV/c (equivalent to 100 keV kinetic energy). A subsequent round of cooling is applied to a de-bunched beam. Once the antiprotons are slowed down enough, up to four bunches can be extracted and transferred to the experiments [11].

Currently, five experiments (ALPHA, ASACUSA, BASE, AEGIS and GBAR) are depending on antiprotons from ELENA. Their collective objective is to study antimatter and its properties. In order to conduct precision studies comparing matter and antimatter, it is essential to have **low energetic antiprotons** suitable for trapping. A key feature of delivering antiprotons with these specifications is the use of **electron cooling** in ELENA, which will be introduced in the next chapter.

2.2 Basics of Beam Physics

This chapter summarizes the basics of accelerator physics and transverse beam dynamics, which are the theoretical foundation for all beam dynamic simulations in this thesis.

In the field of beam physics an **ensemble of particles** that have similar coordinates are referred to as a **beam**. The motion of the particles in electromagnetic

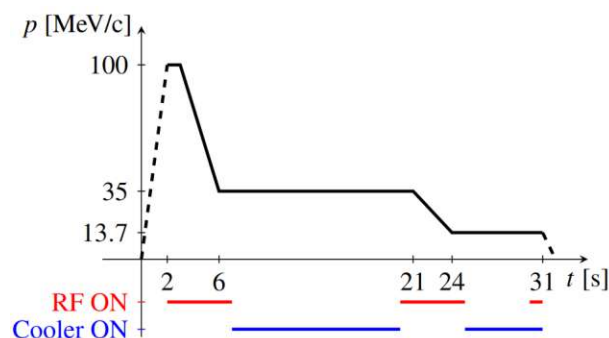


Figure 2.3: Illustration of a typical ELENA antiproton cycle. The solid black line represents the circulating beam; periods highlighted in red and blue indicate operation of RF cavities and electron cooling system, respectively. [11]

fields can be described by a six-dimensional state vector constructed of the positions and momenta [12]:

$$\mathbf{Z} = (x, p_x, y, p_y, z, p_z)$$

2.2.1 Phase Space

The collective space of state vectors \mathbf{Z} is commonly known as **phase space** and the coordinate system depicting the vector is called a **phase space diagram** or plot [12]. In more practical terms, phase space plots represent particle distributions at a specific location (time) in a particle accelerator. Each point on the plot corresponds to a particle and is characterized by its position and momentum.

If the motion in each plane is independent of the others (or only weakly coupled), single phase space plots can be generated. For every spatial direction, there are two variables, where x is the position and p_x is the momentum. For example, the horizontal phase space (x vs. p_x) represents horizontal particle motion [13].

Alternatives to momentum: Trace Space

In beam physics, it is common to replace the momentum coordinate system using a paraxial approximation. This becomes feasible when the transverse momentum components (p_x, p_y) are significantly smaller than the longitudinal momentum (p_z) and p_z can be considered uniform for all particles.

Under this approximation, the transverse angles x' and y' concerning the ideal trajectory can be approximated as $x' = \frac{dx}{dz} = \tan(\alpha_x) \approx \alpha_x$ and likewise for y' . This coordinate system using (x, x', y, y') to characterize transverse motion, as opposed to the conventional (x, p_x, y, p_y) , is called "**Trace space**" [13].

2.2.2 Emittance

In phase or trace space, the volume of the cloud of particles is called **Emittance** (ϵ). It is a property used in accelerator physics that characterizes the spread of particles in both position and momentum within a particle beam. It provides a measure of the area of phase space covered by the beam. Unlike the physical dimensions of the beam, which may vary throughout an accelerator, emittance remains invariant in the absence of dissipative or cooling forces (Liouville's theorem)¹[15].

There are various definitions of emittance and careful consideration must be given to the specific definition in use. The emittance can be defined for each degree of freedom, horizontally, vertically ("transverse plane" i.e., perpendicular to the direction of the beam) and longitudinally.

¹This only applies for a closed system, where the energy is constant (i.e. no interaction between the particles in a bunch, no collisions with remaining gas molecules, no radiation effects, ect.)[14]

Transverse Emittance

Plotted in trace space, one geometric definition for the emittance gives an ellipse. It is usually defined as the area containing 95%² of all the particles in its interior. While the emittance characterizes the size of an ellipse, different conventions exist regarding the relationship between emittance and the ellipse area. The emittance is also the product of the lengths of the semi-axes of the ellipse, resulting in $A = 4\pi\varepsilon$ [16]. Other conventions obstruct the factor 4 or π . Furthermore, it is possible to describe the phase space ellipse dimensions using different physical quantities and distributions. One example is relating the two semi-axes to the **maximum transverse displacement** x_m and to the **maximum transverse angle** x'_m respectively [13, 17].

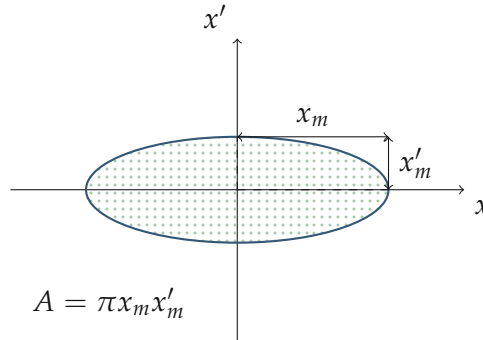


Figure 2.4: Phase space ellipse representation (adapted from [17])

Statistical Emittance

In addition to the geometric convention, there is a statistical interpretation of emittance, which is based purely on the distribution of particles. This definition is commonly employed in particle simulation software, where knowledge of the phase space coordinates of all particles in the beam is available [13].

The root-mean-square (RMS) emittance may be defined as [16]:

$$\varepsilon_{rms,x} = \sqrt{\langle x^2 \rangle \langle (x')^2 \rangle - \langle xx' \rangle} \quad (2.1)$$

assuming that the trace space ellipse is centered at the origin of the (x, x') plane. The angle brackets $\langle \dots \rangle$ represent the arithmetic mean:

$$\langle x \rangle = \frac{1}{N} \sum_{i=1}^N x_i \quad (2.2)$$

Similar to before, it is common practice to multiply $\varepsilon_{rms,x}$ by 4 and denote it as $\varepsilon_{4,rms,x}$.

The emittance can be considered as a quality factor of the beam. Generally it is preferred to minimize the emittance, as small emittance is correlated with the following properties:

- Reduced beam size (smaller range of x values)

²One could also equally use 90% or 99%.

- Reduced velocity spread (smaller range of x' values) [16]

Typically, emittance units for machines like ELENA are expressed in units of π mm rad.

2.2.3 Longitudinal Momentum Spread

In the longitudinal direction a particle's energy or momentum is defined as the difference from the ideal (non-zero) momentum or energy denoted as $\Delta p/p$. This momentum spread is the RMS width of the momentum offset distribution and is dimensionless [13, 15].

2.3 Electron Cooling Theory

This chapter introduces the fundamentals of electron cooling and discusses the cooling system in the ELENA decelerator. In simplified terms, **electron cooling** is a process to reduce the size, the divergence, and the energy spread of a particle beam without removing particles [18]. It was first introduced in 1966 by G.I. Budker at the Budker Institute of Nuclear Physics, Novosibirsk [19]. Since then, electron cooling has been implemented at CERN in LEAR³, AD, and in ELENA, as it is a preferred solution to reduce the emittance and momentum spread for low-energy antiprotons [15].

2.3.1 Motivation for Electron Cooling in ELENA

During the deceleration periods in the ELENA cycle, an **adiabatic emittance blow-up** of the beam occurs — in other words, the occupied phase space increases. This phenomenon results in a subsequent increase in the beam size, which, when nearing the physical or dynamic acceptance limits, leads to undesirable losses [9]. The adiabatic beam blow-up is inversely related to the change in momentum. A particle beam can be conceptualized as an ion plasma circulating in the ring. In the rest frame (moving with the velocity of the ions), the beam energy spread can be characterized as a temperature. The temperature can be viewed as a measure of the beam's quality, with a lower temperature corresponding to higher quality [15]. Processes that increase the beam temperature ("**Heating Effects**") include:

- **Intra-Beam Scattering (IBS):** IBS is caused by multiple Coulomb scatterings of charged particles within the beam itself, both in the transverse and longitudinal planes. As particles pass near each other, Coulomb repulsion causes them to experience small-angle scatterings, leading to changes in their trajectories and momenta. IBS is most pronounced at very low energies, especially for a beam with small emittance, a small momentum spread, and a short bunch length (if bunched). However, the smaller the beam emittance becomes during cooling, the stronger the IBS becomes, which sets a limit on its minimal value [4, 15].

³The Low Energy Antiproton Ring (LEAR) decelerated antiprotons for experiments and was converted into LEIR in 1996 [3].

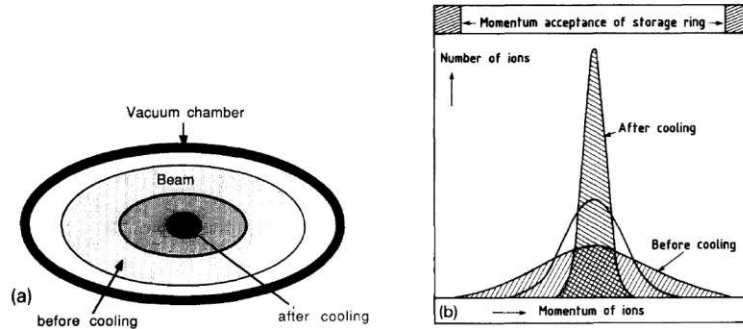


Figure 2.5: Schematic diagram of the effect of beam cooling: (a) on the beam size, and (b) on the momentum spread [18]

- **Space charge effects:** Moving, identically charged particles (in addition to experiencing Coulomb repulsion) generate an electric current and a magnetic field. These fields affect the dynamic behavior of the beam and lead to defocusing [15].
- **Rest Gas Scattering:** Circulating charged particles interact with residual gas molecules in the beam pipe, causing additional heating. This effect is particularly prominent at lower energies [15].
- **Injection mismatches:** During the initial deceleration, potential injection mismatches can contribute to an increase in beam emittance [6].

Table 2.1: Electron Cooler Parameters for ELENA during intermediate and ejection cooling plateau [9]

Item	Value	Dimension
Momentum	35 / 13.7	MeV/c
Electron Beam Energy	355 / 55	eV
Electron Current	5 / 1	mA
B_{Gun}	1000	G
B_{Drift}	100	G
Toroid Bending Radius	0.25	m
Cathode Radius	8	mm
Electron Beam Radius	25	mm
Cooling (Drift) Length	0.75	m
Total Cooler Length	1.93	m

To counteract these heating effects and therefore compress phase space, electron cooling becomes necessary. Figure 2.5 shows the effect of electron cooling on the beam size and momentum. Prior to cooling, the antiproton beam in ELENA has a transverse emittance of $50 \pi \text{ mm rad}$ and a momentum spread of $\Delta p/p = \pm 2 \times 10^{-3}$. After cooling, these beam properties are reduced to $3 \pi \text{ mm rad}$ and $\Delta p/p = \pm 1 \times 10^{-3}$, respectively [4].

As previously mentioned, cooling is applied at two stages in cycle. During the initial cooling plateau, emittance blow-up is primarily caused by injection mismatch and IBS. At the lower momentum, cooling is especially important to ensure that the phase-space characteristics of the extracted antiproton beam are within the specific requirements of the experiments. Improving the cooling process is essential for achieving higher luminosity and therefore increasing the

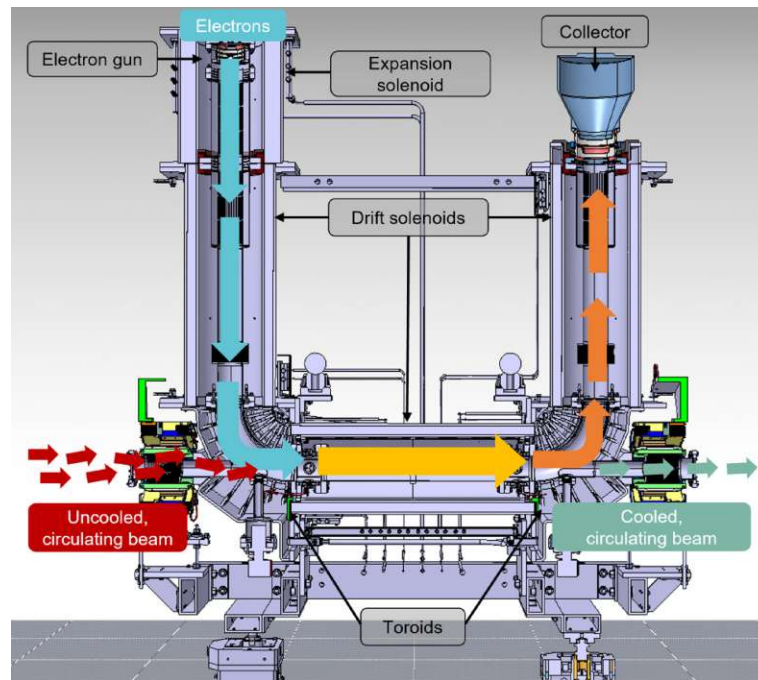


Figure 2.6: Mechanical drawing of the ELENA Electron Cooler, the particle trajectories are illustrated with arrows; adapted from [20]

capture efficiency for the experiments. Improving the precision of measurements through enhanced electron cooling may result in substantial progress in our understanding of antimatter properties.

Nominal parameters of the ELENA electron cooler at intermediate and ejection cooling plateaus are detailed in Table 2.1.

2.3.2 Implementation of Electron Cooling

The principle of electron cooling is based on **superimposing a circulating ion⁴ beam with a co-moving electron beam** over a short, straight segment of the accelerator [15].

Simplified Working Mechanism

Figure Figure 2.6 shows the mechanical layout of the ELENA Electron Cooler. The current ELENA cooler is based on a traditional system, where the electrons are emitted from a thermal gun which is immersed in a longitudinal magnetic guiding field (expansion solenoid).

Monochromatic electrons are produced in an **electron gun** and are accelerated electrostatically to almost the same average velocity as the circulating beam. The electrons undergo a 90° bend and are guided to overlap with the circulating antiprotons over a distance of 0.7 m (cooling length l). In this section the cooling process happens: the ion particles have a variety of different angles and velocities, while the electrons are all moving with the same velocity. If observed

⁴To differentiate between electrons and particles subjected to electron cooling, the term "ion" is used for any particle, including antiprotons.

from a frame moving with the velocity of the electrons (e.g. electrons are at rest, "rest frame"), the ions simulate the behavior of **particles in a hot gas**. One can associate a **temperature** T_i to the ion gas, which is linked to the **width of the ion velocity distribution**, and similarly for the electrons temperature T_e . Collisions occur between the ions and electrons, the ions either gain or lose energy through **Coulomb interactions** with the electrons. As the electrons are constantly renewed, energy is continually extracted from the electron-ion system, causing the ion beam to undergo a reduction in temperature, as the energy of the thermal motions is transferred to the colder electrons. Eventually, the ion beam will assume T_e . After having served their purpose in the cooling section, the electrons are bent again and reabsorbed in the collector.

The cooling process can be seen as a **thermal equilibration** between the hot ion beam and a cold electron beam [9, 15]. A simple analogy to electron cooling would be the heat exchange in a refrigerator, where the electrons act like a cooling liquid, and the food in the fridge are the ions, that need to be cooled.

2.3.3 Electron Cooling Time

Electron Cooling has been extensively discussed in research [18]. The calculation of the cooling time τ is not trivial and typically requires numerical methods. However, the **cooling rate** $1/\tau$ can be estimated from the following simplified expression:

$$\frac{1}{\tau} = \frac{Q^2 L_c r_e r_p}{k A e} \frac{j \eta_c}{\beta^4 \gamma^5 \Theta^3} \quad (2.3)$$

where:

- $k = 0.16$ (constant depending on distributions of ions and electrons),
- $Q = -1$, $A = 1$ (charge and mass number of the ions, here antiprotons),
- $\eta_c = 0.023$ (ratio of cooling length to ring circumference: 0.7 m over 30 m at ELENA),
- β (velocity of the ions normalized to the speed of light),
- γ (Lorentz factor of the ions),
- $L_c \approx 10$ (Coulomb logarithm),
- $r_e = 2.8 \times 10^{-15}$ m (classical electron radius),
- $r_p = 1.54 \times 10^{-18}$ m (classical proton radius),
- j [A m^{-2}] (current density of the electron beam),
- Θ (r.m.s. angular spread between the electron and ion beam) [4].

Cooling theory gives the following simple conclusion: the lower the cooling time, the faster the ion beam aligns with the electron beam and the more effective is the cooling process. From the relation above it is clear that a number of machine and cooler parameters can influence the cooling time, but only a few are controllable⁵: j , Θ and η_c [4].

⁵The cooling length is pre-fixed and the current density needs to be adjustable for ELENA operations.

The most effective possibility to decrease the cooling time, is by improving the electron-ion beam alignment (as Θ is directly proportional to the cooling time by the power of three)⁶ i.e. reducing electron beam energy spread.

Based on these arguments, it can be concluded that the **electron beam temperature** is a major influence on the cooling time [9]. In order to achieve fast and efficient cooling, special attention must be paid to the design of the electron gun and the quality of the magnetic field that guides the electrons from the gun to the collector [4].

2.3.4 Cooler Magnet System

The overall electron cooling system is embedded in a longitudinal magnetic field to allow for the desired beam orbits and prevent beam blow up from Coulomb repulsion [18]. It is comprised of three main magnets: the gun solenoid, two drift solenoids and the collector solenoid.

Of particular importance is the **expansion solenoid** (see Figure 2.6) in which the electron gun is immersed in. Its geometry is similar to the gun solenoid, but the magnetic field is 10 times higher. Because the longitudinal magnetic field B_{\parallel} is proportional to the transverse beam energy E_t , following $\frac{E_t}{B_{\parallel}} = \text{const}$, the difference in the magnetic field can be used to lower the beam transverse temperature and increase the beam size. In this way, adiabatic expansion can be achieved, which is important for effective cooling, aiming to reduce the transverse beam temperature to 10 meV.

Aside from these magnets, the system includes two toroidal magnets that are used to bend the electron beam. Various correction coils are installed to provide finely tuned field optimization [4, 6].

2.4 Electron Emission Theory

This chapter outlines the behavior of electrons in metals and discusses the three major mechanisms of electron emission, i.e. thermal, photoelectric and field-induced. The quantum mechanical tunneling effect required for field emission is explained using the Fowler-Nordheim theory.

Electrons in metals

The theory of electron emission from metals relies on two fundamental assumptions. Viewed in the **band theory** of solids, electrons in the energy band of metals can be considered as loosely bound electrons that are acting as a free electron gas. The electronic states within the metal adhere to the Sommerfeld-Bethe model, conceptualizing the metal as a box with a constant inner potential V . Near to the surface of the metal, the potential rises, forming a wall that

⁶It is noteworthy to mention that the angular spread for electrons includes more complex dependencies, for example the electron beam temperature, different velocity distributions and drift velocities.

is preventing the electrons from spilling out – called the **potential barrier** or vacuum barrier⁷.

Inside the metal, a free electron with an energy inside the energy band can be described quantum mechanically as a standing wave with nodes at the surface. According to the Pauli principle, the energy states are filled up starting from the ground state (the lower edge of the conduction band) and culminating at the **Fermi level** E_F , the highest energy state that electrons occupy⁸. The height of the barrier with respect to the Fermi level is termed the **work function** ϕ , a material property specific to the cathode. It is equal to the energy required to excite the electron from Fermi level to the vacuum level to get liberated. As temperature rises, electrons can be excited to higher energy levels. To quantify the probability of discovering an electron in a specific state, particle statistics (e.g. Fermi-Dirac statistics) need to be considered [21]. All thermionic functions adhere to the Fermi-Dirac distribution, with further elaboration available in other literature [22].

2.4.1 Electron Sources

The generation of particle beams by emission depends strongly on the particle type and the characteristics needed for the specific application. Electron beams are formed by extracting electrons from a donor material called **cathode**. The process of donating electrons from a material is referred to as **emission** phenomena [23]. All structures (solids, gases, plasma, metals, etc.) that are composed of electrons or ions can theoretically emit charged particles. In order to be emitted, the electrons need to overcome the potential barrier. This can be accomplished either by providing extra energy to the electrons, enabling them to exit the material, or by reducing the work function [12].

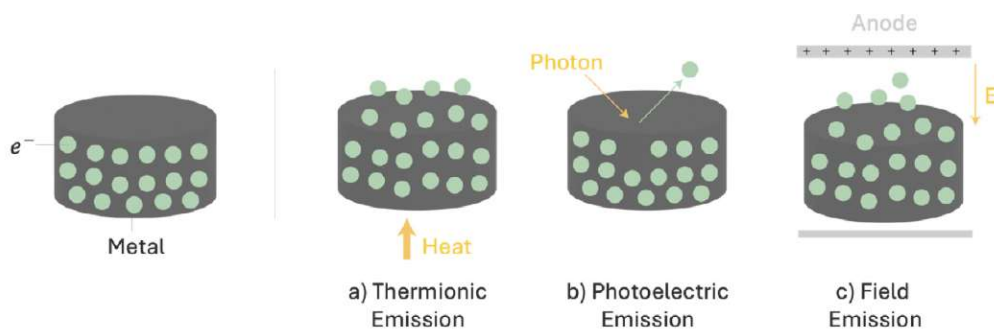


Figure 2.7: Three main mechanisms of electron emission: (a) Thermionic emission via heating, (b) Photoelectric emission by photon-electron interaction and (c) Field emission due to an applied electric field E .

The three main mechanisms inducing electron emission are:

1. **Thermionic Emission:** To obtain thermionic emission, a metal is heated, which allows the electrons to become more energetic as they obey Fermi-Dirac statistics. A considerable fraction of electrons gain sufficient kinetic energy to overcome the vacuum barrier and exit the material [21]. The

⁷At the vacuum level the electron is free from the solid, $E_{pot} = 0$ [21]

⁸at absolute zero temperature.

current density is directly proportional to the applied cathode temperature T_c . In other words, the greater the temperature, the greater the amount of thermionic emission. The electrons follow a Maxwellian shaped velocity distribution with a temperature T_e equal to T_c [18]. The extracted electrons form a cloud near the surface are pulled away and then accelerated to the desired energy by an electric field.

2. **Photoemission:** When photons with sufficient energy strike the surface of a metal (e.g., sodium, potassium, or cesium), the energy of the photons is transferred to free the electrons within the material. These electrons, subsequently emitted from the surface, are called photoelectrons [23].
3. **Field Emission:** When placing an positively (relative to the source) charged anode near the surface of a material, an electric field is generated. If the applied voltage is high enough, electrons can escape through quantum tunneling (as elaborated in [subsection 2.4.2](#)) [12, 23]. While pure field emission ideally occurs at absolute zero temperature ($T = 0$ K), practical conditions involve finite temperatures, leading to what is known as **cold field emission**. Typically, cold FE takes place at a metal-vacuum surface, but it can also occur with semi-conductors, liquids, polymers or most importantly in this scope **Carbon Nanotubes(CNTs)** [24].

2.4.2 Fowler-Nordheim Theory

Field emission is based on the quantum mechanical tunneling of conduction electrons subjected to an applied electric field. The first successful model of electron emission from metals was proposed by Fowler and Nordheim in 1928 [25]. The **Fowler-Nordheim (FN)** theory solves the Schrödinger equation that describes the transmission probability for electrons near E_F tunneling through a triangular barrier. The actual mathematical derivation of the **field emission current density** j_F as a function of the work function ϕ and the local field F is briefly outlined in the following section [26].

Assumptions

The FN theory makes multiple assumptions to simplify the field emission model, which are summarized below [27, 28, 26]:

- The emitter is modeled by the Sommerfeld model with a single metal conduction band in thermodynamic equilibrium at $T = 0$ K.
- The emitter has a flat, planar surface and its work function is independent of the external electric field ($d\phi/dF = 0$).
- The vacuum potential barrier is considered to be triangular and only one-dimensional tunneling is considered.
- The Wentzel-Kramers-Brillouin approximation is used to determine the electron tunneling probability.

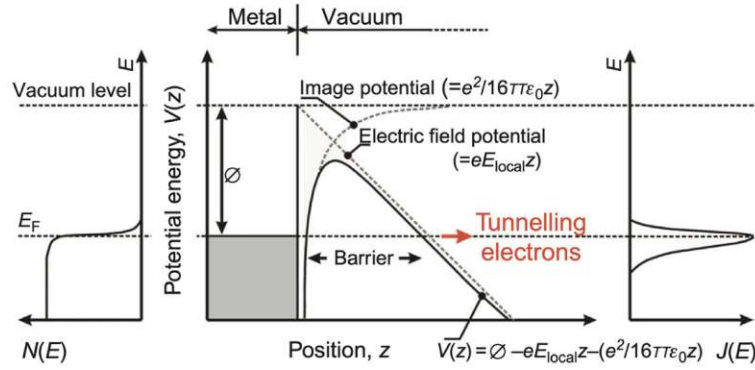


Figure 2.8: Field emission potential diagram at the metal-vacuum interface. The bending of the surface barrier is due to the combined effect of the applied electric field and the image potential, resulting in the effective potential $V(z)$. On the left, $N(E)$ illustrates the fluctuations in electron density within the emitter, while the current density $J(E)$ is a function of energy E of the tunneled electron and is represented on the right side [30]

Wave equation and potential $V(z)$

The 1D time-independent Schrödinger equation for the tunneling electron is defined as:

$$-\frac{d^2\Psi(z)}{dx^2} - k_0^2(E_f - V(z))\Psi(z) = 0$$

where $\Psi(x)$ is the wave function, $V(z)$ denotes the potential energy experienced by the electron at position z , E_f signifies the total forward energy of the electron and $k_0 = \left(\frac{2m_e}{\hbar}\right)^{1/2} \approx 5.123 \text{ eV}^{-1/2} \text{ nm}^{-1}$ is a derived universal constant [29]. The complete representation of the Fowler-Nordheim potential is depicted in Figure 2.8, with the effective potential energy $V(z)$ given by⁹:

$$V(z) = \begin{cases} 0 & \text{for } z < 0 \\ \Phi - eFz - \frac{e^2}{16\pi\epsilon_0 z} & \text{for } z > 0 \end{cases}$$

The first constant term Φ for the half vacuum space $z > 0$ corresponds to the work function of the material. Then, there are two effects that together result in the product of a triangular barrier. The first linear term accounts for the external homogeneous electric field $|\mathbf{E}| = F$ that is applied and reduces the potential energy by the amount of $-eFz$. $-\frac{e^2}{16\pi\epsilon_0 z}$ is the Coulomb potential caused by an image charge of opposite sign, which arises from the attraction of the induced positive charge in the metal [22].

From Figure 2.8 a few conclusions can already be made: A small fraction of cold trapped electrons close the Fermi energy E_F can escape through the surface tunnel barrier, if it is less than a few nanometers. By increasing the applied electric field, barrier narrowing is induced and the number of emitted electrons is increased [30].

⁹ z is the distance from the surface

Fowler-Nordheim equation

After solving the Schrödinger equation and applying appropriate approximations and boundary conditions and then integrating tunneling-current contributions from all occupied free-electron states, field emission can be described by the Fowler-Nordheim (FN) equation [26].

As indicated in [30], the **field emission current density** j_F can finally be expressed as the conventional FN equation:

$$j_F(F) = \left[\frac{A_{FN}}{\phi \cdot t(s)^2} \right] F^2 \exp \left(-B_{FN} \cdot v(s) \cdot \frac{\phi^{3/2}}{F} \right) [\text{A m}^{-2}]$$

where the first and second FN constants are

- $A_{FN} \equiv \frac{e^3}{8\pi h} = 1.54 \times 10^{-6} \text{ A} \cdot \text{eV}/\text{V}^2$
- $B_{FN} \equiv \left[\frac{8\pi}{3e\hbar} (2m_e)^{1/2} = 6.83 \times 10^9 \text{ eV}^{-3/2} \text{V}/\text{m} \right]$

and the Nordheim elliptical functions, depending on the slope factor s are approximated by:

- $t(s) = 3.79 \times 10^{-5} \left(\frac{F^{1/2}}{\phi} \right)$
- $v(s) = (0.956 - 1.062s^2)$

To simplify calculations, $t(s)$ and $v(s)$ are frequently set to unity, resulting only in minimal loss in accuracy leading to:

$$j_F(F) = \left[\frac{A_{FN}}{\phi} \right] F^2 \exp \left(-B_{FN} \cdot \frac{\phi^{3/2}}{F} \right) [\text{A m}^{-2}] \quad (2.4)$$

2.4.3 Generalized FN-equation

The generalized Fowler-Nordheim equation is frequently used in literature for fitting experimental data due to its streamlined form compared to Equation 2.4. It describes the emission behavior well enough for most emitters [31]:

$$J(E) = AE^2 \exp \left(-\frac{B}{E} \right) [\text{A m}^{-2}] \quad (2.5)$$

The applied electric field E can be approximated using the anode-cathode voltage V and inter-electrode separation d by $E \approx \frac{V}{d}$ [32]. Constants A and B are defined by the material properties and experimental conditions. By fitting data to this exponential curve, it is possible to determine key parameters for evaluating emission performance and comparing different emitters or conditioning methods. Three commonly used criteria for good emission are a low **turn-on electric field** (E_{on}), a low **threshold electric field** (E_{thr}) and a high **maximum current density** (J_{max}). Definitions in the literature vary largely; E_{on} and E_{thr} are typically defined at emission current densities of 0.01 mA cm^{-2} and 0.1 mA cm^{-2} , respectively [32].

2.5 Carbon-Nanotubes (CNTs)

Introduction

Carbon-Nanotubes (CNTs), are an allotropic form of carbon within the fullerene family. While the formal credit for the discovery of CNTs is often attributed to Iijima in 1991 [33], the initial observation was actually made by Radushkevich and Lukyanovich in 1952 [34]. Remarkably, the exceptional mechanical and chemical properties of CNTs have been utilized for the strength of Damascus steel, dating back to the seventeenth century.

Since then, CNTs have emerged as an adaptable material used across a range of scientific and technological fields. There has been extensive research into the properties, synthesis and numerous potential applications of CNTs, including solar cells, X-ray sources, semiconductor devices, flat-panel field-emission displays and many more [7, 30].

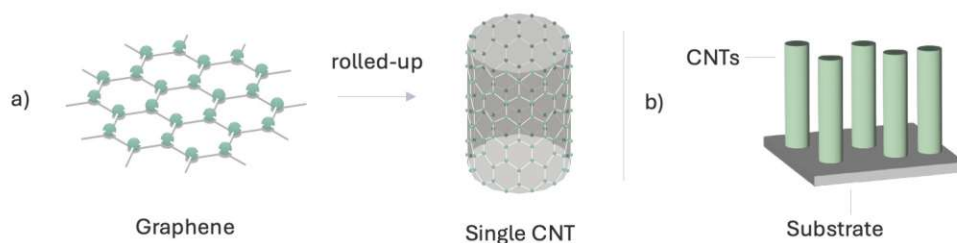


Figure 2.9: Schematics: (a) A graphene sheet rolled up to form a single CNT, (b) Vertically aligned CNTs on a substrate.

Classification of CNTs

CNTs exist in two main forms: **Single-wall** CNTs (SWCNTs) and **Multi-walled** CNTs (MWCNTs). SWCNTs are made of one single sheet of graphene rolled up in a specific direction to form a tube (see Figure 2.9). The single-atom thick sheet consists of hexagonally latticed carbon atoms with a strong covalent bonding. Each hexagon shares two atoms with an adjacent hexagon giving rise to the typical honeycomb structure. The ends of the tube can remain open, bond to other atoms or form fullerene-like hemispherical caps [35, 30]. **Chirality** is another major parameter that allows the classification of CNTs into three different types depending on how the sheet is rolled up, namely the armchair, zigzag and chiral type. SWCNTs can exhibit either metallic or semiconducting behavior based on their chirality¹⁰.

MWCNTs consist of several concentric, coaxial graphene cylinders, each with its own chirality. The interlayer spacing between the cylinders is 0.344 nm on average and thus is slightly larger than the interplane spacing in graphite (0.335 nm) [9]. The diameters of MWCNTs range from 2 nm to 500 nm, with lengths spanning from 50 nm to a few centimeters [30]. Most MWCNTs have been shown to exhibit metallic properties. Studies comparing SWCNTs and

¹⁰Armchair types possess metallic electrical properties; the rest have semiconductor characteristics [36]

MWCNTs have demonstrated that MWCNTs tend to be more resistant, with SWCNTs exhibiting a degradation rate that can be ten times higher [9].

Properties of CNTs

CNTs possess an array of extraordinary chemical, mechanical, electrical and thermal properties that contribute to their widespread applicability. Notably, CNTs exhibit a Young's modulus (measure of material stiffness) approximately five times larger than steel with a much lower mass density. The strength of the carbon-carbon bond makes them one of the strongest and stiffest materials known. They have an ultrahigh **aspect ratio** ($> 10,000$) (length over diameter) and a good chemical stability. Their thermal conductivity at room temperature can reach up to $3000 \text{ W m}^{-1} \text{ K}$, which is comparable with diamond. Other properties include high flexibility (significant bending without damage), very high tensile strength (50 times higher than that of steel), electrical conductivity and most relevant in this thesis, great electron field emission characteristics [7].

Most properties mentioned so far relate to the intrinsic features of individual CNTs. However, they can be fabricated into macroscopic assemblies and architectures (e.g. fibers, arrays, thin films ect.), where some properties are not necessarily directly transposable, but can bring out other advantages [35]. Many approaches for CNT synthesis exist, the three mainly methods used include **laser ablation**, **electric arc discharge** and **chemical vapor deposition (CVD)** [30].

2.5.1 CNT based Field Emission

CNTs are exceptional candidates for cold cathode field emission applications due to their special characteristics. The combination of a high aspect ratio and a small tip curvature allow for a highly concentrated electric field in the vicinity of the tip, leading to a large **field enhancement factor** β . β is given by the ratio of length and radius of the emitter and can be used to reflect the field emission performance of CNT architectures. Assuming an applied electric field E at the tip, the enhanced local field can be defined as $F = E \cdot \beta$ [8]. Then Equation 2.4 can be written as:

$$j_F = \left[\frac{A_{FN}}{\phi} \right] (E_{app} \cdot \beta)^2 \exp \left(-B_{FN} \cdot \frac{\phi^{3/2}}{E_{app} \cdot \beta} \right) [\text{A m}^{-2}] \quad (2.6)$$

Compared to a planar emitter, a nanotip emitter effectively reduces the barrier by a factor of β . This reduction increases the probability of tunneling and consequently, the emission current [37]. In other words, the same electric field E results in a higher effective field and therefore a higher current density than a non-nanoscale-tip emitter.

In order to extract more parameters from the experimentally obtained current density plots, a so called Fowler–Nordheim plot is often utilized. The exponential relationship described in Equation 2.6 is used to plot $\ln(j_F/E^2)$ versus $1/E$. In an ideal FN process, this plot is linear, confirming that quantum

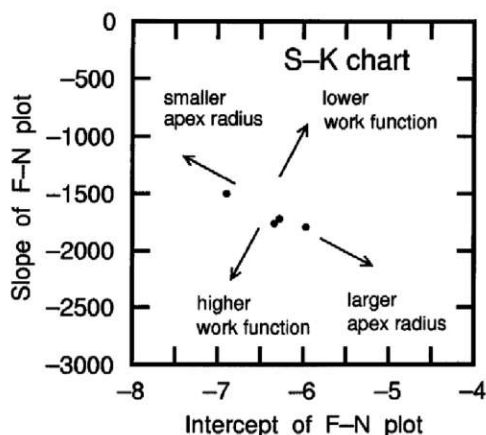


Figure 2.10: Example of a Seppen-Katamuki plot with interpretation of FN characteristics [38]

tunneling dominates the emission, where as deviations indicate additional adverse influences. To further analyze the contributions of β and ϕ to the field emission performance, a Seppen-Katamuki (SK) ¹¹ plot is commonly used. In a SK plot, the abscissa represents collected intercept of the FN plot, while the ordinate represents the slope m [39]. β can be calculated from the slope using $m = -\frac{B_{FN}\phi^{3/2}}{\beta}$ [2]. Furthermore, to get a very rough approximate of the emitter tip radius r , the Gomer formula $\beta = 1/5r$ can be used.

An example of a SK plot and how to interpret the FN characteristics it can be viewed in Equation 2.6. The upper left indicates a smaller emission area/apex radius and the lower right indicates a larger emission area/apex radius. The upper right area represents a lower work function, while the lower left indicates a higher work function. SK plots are specifically practical to compare different cathodes and changes in emitter geometry [38].

Theoretically, because electron emission primarily occurs at the sharp tips of carbon-nanotubes, the FN theory's assumption of a smooth surface is no longer applicable. Nonetheless, it has been established that the FN equation can still verify experimental data within certain current ranges [9].

2.5.2 VACNTs

Previous studies concluded that great field emission performance can be achieved with **vertically aligned CNTs (VACNTs)**. VACNT consist of uniform, vertically oriented CNTs tethered perpendicular to a rigid, metallic substrate enabling connection to a power supply (see Figure 2.9) [9]. VACNTs exhibit an exceptionally low turn-on fields 1 to 3 V μm^{-1} , a stable emission current, fast switch-on time and high field emission current density ($> 1 \text{ A cm}^{-2}$) [9, 40]. A current density of 80 mA cm^{-2} under an applied electric field of 3 V mm^{-1} was reported using a VACNT field emitter [41]¹².

¹¹In Japanese, "seppen" means intercept and "katamuki" means slope [38].

¹²These results were obtained with a field emitting area of 4.03 cm^2

Typically, VACNTs are made using **chemical vapor deposition**¹³. VACNTs can be fabricated as full forest arrays or as freestanding, periodically patterned arrays, where the CNTs are located on specific areas¹⁴.

2.5.3 Factors affecting FE efficiency in VACNTs

Many factors can play a role in the attempt to enhance FE in CNTs, but due to space restraints, only for this scope relevant features will be discussed. Field emission efficiency depends on various different parameters namely: type of CNTs; tube diameter; tube length; growing mechanism; substrate type; open or closed cap; density, impurities and orientation of the tubes; and inter-tube spacing [9]. Three possible strategies to reduce the VACNT degradation during emission and thus improve their FE efficiency and stability are discussed below.

Efforts to reduce ϕ and to produce high-performance CNT emitters include decorating CNTs with low work function materials (e.g. Cs, MgO, ZnO) and doping with heteroatoms, such as B, Li or N [5]. Other options include growing CNTs on metallic substrates like steel or copper possibly leading to a better electrical contact compared to conventional silicon (Si) substrates [43, 42].

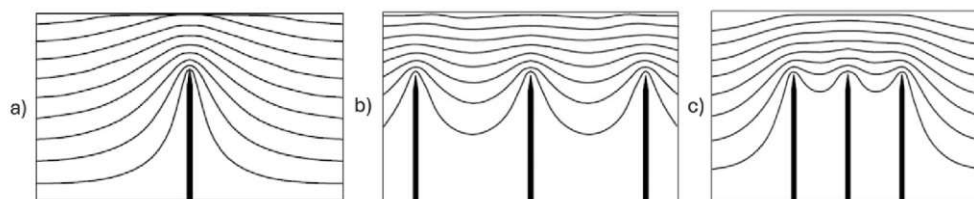


Figure 2.11: Spatial distribution of the electric potential near CNTs for various inter-tube distances. (a) Single CNT, (b) Three widely spaced CNTs and (c) Three moderately spaced CNTs. The closer the nanotubes, the lower the electric field enhancement factor [44].

Another approach is varying the density of CNTs to improve FE. With highly densely packed VACNTs a so called **screening effect** occurs: the electric field of the neighboring CNTs lowers the average field enhancement near their tips as the field lines struggle to fully penetrate. As β decreases with decreasing inter-tube distance, according to Equation 2.4 screening¹⁵ adversely affects FE, especially for large or dense emitters [7]. Thus, high density results in the reduction in the emission current. Conversely, as the emitted current depends on the number of emission sites, emission is poor for low density of CNTs [9, 42]. It has been reported that optimal emission performance is achieved when the spacing between neighboring CNTs is approximately two times the CNT

¹³CVD is a process used to deposit solid material from a gaseous phase through chemical reactions with heated substrates. The processes involve two fundamental steps: (1) the preparation of a catalyst bed and (2) subsequent growth facilitated by the decomposition of reactant gases. Several types of CVD exist, for CNT growth, mainly Thermal- and Plasma-enhanced CVD are used. CNT length and diameter can be controlled by the deposition time and thickness and type of catalyst thin film, respectively [9, 30].

¹⁴Used position controls for the catalyst pattern realisation are for example electron beam lithography, nanosphere lithography or nanoinkjet deposition [42, 30]

¹⁵Screening is more pronounced for CNTs in the middle of an array, gradually diminishing toward the edges [9].

height [42]. Considering taller CNTs with higher aspect ratio, theoretically more field enhancement is achievable. However, in an array configuration, longer nanotubes require larger spacing to limit screening [9].

Different VACNTs patterns were designed to improve FE and reduce screening effects to obtain optimal field enhancement. Excellent performance was given by the **squared-islands pattern** and the **honey comb pattern**, where the CNTs are placed in a hexagonal arrangement, resembling a honeycomb structure when viewed from the top. The lower overall density compared to a full forest, while still allowing for a good space coverage, makes these patterns a very effective mean to balance the previously discussed factors [9, 40].

Finally, it is of essential relevance to consider the damage of the CNTs during emission, as the **stability** and **durability** of the cathode is one of the most important prerequisites. The stability can be affected by various factors, such as failure of the CNT substrate adhesion layer, the presence of residual gases causing ion bombardment and ionization processes and local Joule heating leading to changes in the structure of the nanotube tip [5]. Individual protruding CNTs emit more electrons and eventually overheat as the temperature depends on the emitted current. Joule heat accumulates and can melt the CNTs, leading to failure. Therefore, high uniformity — where the height of CNTs is evenly distributed — is favorable, as it helps to prevent burnt tips and ensures a stable current [45].

2.6 Electron Guns

In this section, electron guns are presented and the requirements for the ELENA electron gun are discussed. Various design considerations regarding the electron gun are also explained. It is important to emphasize that while the focus of this work is on the development of an electron gun for low-energy cooling in ELENA, these results and findings can be used for a variety of applications. A more extensive discussion of medical applications will follow in later sections.

2.6.1 Basic theory of Electron Guns

As already mentioned in subsection 2.3.2, the electrons required for cooling are generated and accelerated to the necessary kinetic energy $E_0 = m_e c^2 \cdot (\gamma - 1)$ ¹⁶ using an electron gun.

The simplest (thermionic) electron gun configuration is comprised of two electrodes: the **cathode** and the **anode**. The anode is maintained at a positive potential relative to the cathode and features a small opening to allow the extracted beam to pass through. However, this is not an optimal arrangement¹⁷, thus a **triode system** is often preferred. A third electrode placed between anode and cathode, commonly known as the **grid**, is held at a more negative

¹⁶Here, c is the speed of light in a vacuum, m_e is the rest mass of the electron and $\gamma = \frac{1}{\sqrt{1-v^2/c^2}}$ is the Lorentz factor, where v is the velocity of the electron.

¹⁷A basic diode arrangement has some drawbacks, for example that too many electrons hit and thus heat the anode. The current can only be altered by changing T_c , which is naturally a very slow process.

potential compared to the anode. Its primary purpose is preventing electrons from striking the anode and exerting a focusing and controlling influence on the electron beam [22].

2.6.2 Gun design considerations for Electron Cooling

As said before, **efficiency** of cooling relies strongly on the **quality of the electron beam** and how well aligned both beams are [18]. Therefore, special attention has to be given to the electron gun design and its cathode. The goal is to achieve the **lowest possible cathode temperature** i.e. the smallest transverse energy spread of emitted electrons. In order to optimally select a gun for a specific purpose, a thorough evaluation of the various requirements and limitations is necessary, which will be discussed below.

Two key metrics of concern for cathodes in general are the emitter's **lifetime** and **stability**. Lifetime is defined as the duration during which the emitter can maintain its performance, often assessed through constant or pulsed measurements. Stability, on the other hand, measures the fluctuation in emitted current over time at a fixed voltage [28].

Requirements for the ELENA Electron Gun

The electron gun in ELENA is placed in a solenoidal magnetic field of 1000 G to avoid Coulomb repulsion among the electrons in the beam, as mentioned before [18]. It must function continuously throughout an entire operational period, which typically is around one year. Furthermore, the gun should produce a cold beam, with a transverse temperature of $T_{\perp} < 0.1$ eV, a longitudinal temperature of $T_{\parallel} < 1$ meV and an electron density of $n_e \approx 1.5 \times 10^{12} \text{ m}^{-3}$.

Advantages of cold cathode sources

Currently, the ELENA cooler employs a classic thermionic cathode, which is electrically heated to approximately $T_c = 1200$ °C. Conventional cathodes are typically made from metals with low work functions¹⁸, such as tungsten coated with an electron-emitting material like barium oxide (BaO). Even though thermionic cathodes can be operated straightforwardly, are simple to manufacture and have a long lifetime, there are a few limitations. In case of the current ELENA cathode, the high temperature limits the minimum transverse energy spread of the beam to 0.1 eV. In practice, this spread can increase significantly further from the central beam region, due to the effects of the electron gun's electrodes and the beam's tail effect. Thermionic cathodes are commonly used where the high temperature does not limit the machine performance [22, 18].

Considering the demands of the ELENA cooler, exploring the use of a colder source could provide significant improvements in performance and efficiency. One option would be photoemission-based guns, but they rely on complex experimental setups due to the laser system. Other downsides include the

¹⁸A small work function allows electron emission at lower temperatures.

poor stability of the emitted current and the relatively short lifespan of the photocathodes, making them less suitable for this study [9, 23].

However, **Field Emission Electron Guns (FEGs)** could present an exciting alternative. In comparison to thermionic guns, FEGs rely solely on a strong electric field, avoiding complications associated with heating. Therefore, cold electron emission could provide a more uniform transverse energy spread [9].

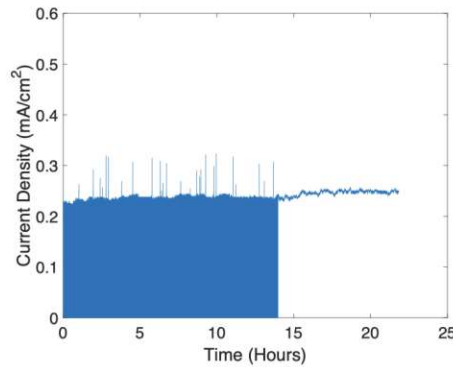


Figure 2.12: Emission stability test in switching mode for a honeycomb-like array with an applied electric field of $E = 2 \text{ V}/\text{m}$. The test was performed for around 14 hours in switching mode, followed by DC mode to compare stability [9].

FEGs offer several further benefits over thermionic cathodes, including higher brightness and lower power consumption [22]. Additionally, FEGs have demonstrated the ability to produce a stable and focused electron beam for over 1500 hours and reaching high enough current densities. Galante [9] proved that current densities up to 2 mA cm^{-2} are possible depending on the applied electric field. CNT based FEGs have also shown to operate effectively in fast switching mode, which is necessary for ELENA operation. As shown in Figure 2.12, the emission during switching remained stable over a 14-hour period, with only a few current peaks. In this mode, the cathode is switched on for 15 seconds, followed by a 15-second pause, reflecting the cooling plateaus in the ELENA cycle. After switching to DC mode, the current stability remained and further switching for an additional 25 hours showed no degradation. These preliminary results confirm the feasibility of FEGs for ELENA. Therefore, while thermionic cathodes are currently in use due to their robustness and simplicity, the potential benefits of transitioning to FEGs warrant careful consideration for future upgrades [18, 6].



Die approbierte gedruckte Originalversion dieser Diplomarbeit ist an der TU Wien Bibliothek verfügbar
The approved original version of this thesis is available in print at TU Wien Bibliothek.

3 Experimental Study

3.1 The Electron Gun

The reliable operation of an electron gun depends on many technological details, for which no exact theory exists and which often cannot be fully investigated by experiments. Thus, a successful electron gun design requires much practical experience as well as knowledge of the underlying theory.

3.1.1 Components of the Electron Gun

Previous studies [9] developed a preliminary design for a **dual-gridded electron gun based on a cold cathode CNT sample**. It relies on a triode configuration where both the extracting anode and the third electrode are referred to as grid 1 and grid 2. In this configuration the silicon wafer, on whose surface the CNTs are grown, is used as a cathode with a negative applied voltage. The voltage on grid 1 is responsible for creating the local electric field that extracts the electrons from the CNTs. Grid 2 is usually grounded¹ so that the electrons can be transported downstream with the required beam energy (for ELENA operation 355 eV). The two grids were manufactured by MicroCreate BV using a highly n-doped round silicon wafer with a thickness of 100 μm and a diameter of 4 inches. The wafer was thinned down to 50 μm in a central area where a rectangular hole pattern measuring $3 \times 3 \text{ cm}^2$ was created. The mesh consists of 15 μm square holes separated by 3 μm walls (see [Figure 3.1](#)).

Additionally, two MACOR®² ring-shaped spacers are used for insulation between cathode/grid 1 and grid 1/grid 2. The spacers inner diameter limits the beam size and act as a short drift tube for the beam. The final component is a focusing electrode, an aluminum ring with a triangular-shaped cross-section. It helps maintain straight field lines and keeps the transverse energy of the emitted beam low. All edges of metal surfaces exposed to high voltage are rounded, to reduce the risk of electrical discharges and arcing. HV coaxial feedthroughs in the upstream flange were used to make electrical connections to the power supplies or multimeters.

All these components, collectively referred to as the “emitter region”, are stacked and secured with screws. A simplified illustration of the working principle of the emitter region can be viewed in [Figure 3.2](#). After the focusing electrode, the beam is directed through an Einzel lens system (see [subsection 3.1.3](#)).

3.1.2 Challenges and Optimization of the Gun Design

The electron gun prototype, initially proposed in previous studies [9], underwent several modifications to address various issues encountered during testing.

¹However, a positive voltage can also be applied in order to enhance electron emission, if needed.

²MACOR® is a machinable glass-ceramic material with an electrical insulation [46].

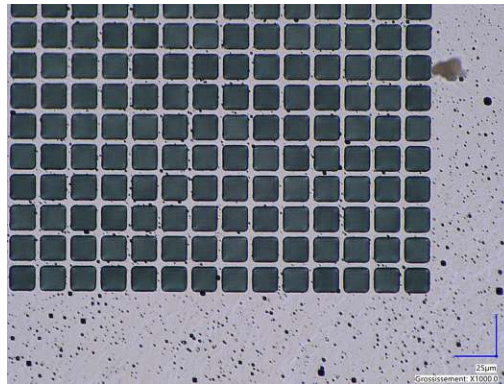


Figure 3.1: Optical microscopy of the grid; showing a corner of the meshed area, with the grid comprising of 15 μm square holes with 3 μm walls

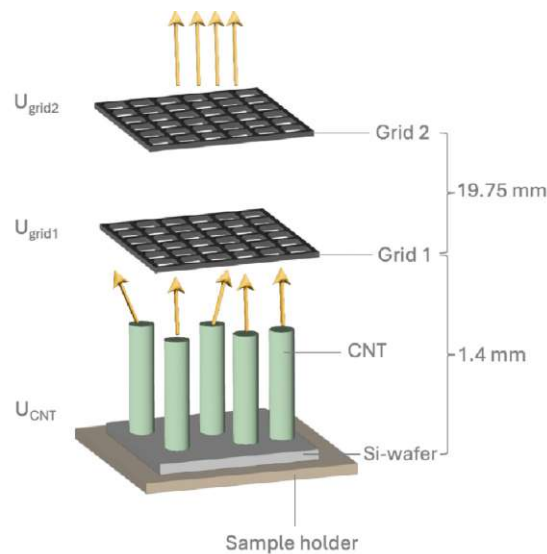


Figure 3.2: Schematic illustration of the CNT-based electron gun working principle: The sample holder contains the CNT sample grown on a Si-wafer. Three voltages are applied: U_{CNT} , U_{grid1} and U_{grid2} to enable tunneling. The emitted electrons pass through grid 1 and grid 2, which are placed 1.4 mm and 19.75 mm above the CNT sample, respectively. The arrows indicate the direction of the emitted electrons.

For example, the original gun design had a vacuum breakdown at a few kilovolt applied voltage. Additionally, silver glue was used to secure the supply copper/Kapton® wire between the copper sample holder and the bottom of the sample, but this did not provide sufficient surface contact to properly conduct the applied voltage.

To overcome these problems, a few changes were made to improve the operational stability and insulation between components. As the gun design has to meet Ultra High Vacuum (UHV) and High Voltage (HV) requirements and the electrodes are very close together, finding the best configuration was not trivial. A new PEEK³ sample holder was designed to significantly reduce the risk of flashes and vacuum breakdown at higher voltages. The voltage was applied using a screw at the bottom of the sample, with aluminum foil that helps to ensure an electrical connection to the entire surface. PEEK nuts and screws with a small groove along the longitudinal side were used to avoid gas pockets

³Polyetheretherketone (PEEK) is a high-performance thermoplastic [47]

that could prevent good vacuum performance. This also reduced the risk of sparking between the conducting elements. Additionally, thicker wires shielded with MACOR® beads, were added to improve insulation.

Three Vespel®⁴ inlays (see Figure 3.6) were produced to house smaller sized samples (1 cm², 4 cm² and 9 cm²) within the sample holder. The final electron gun prototype can be viewed in Figure 3.3 and Figure 3.5.

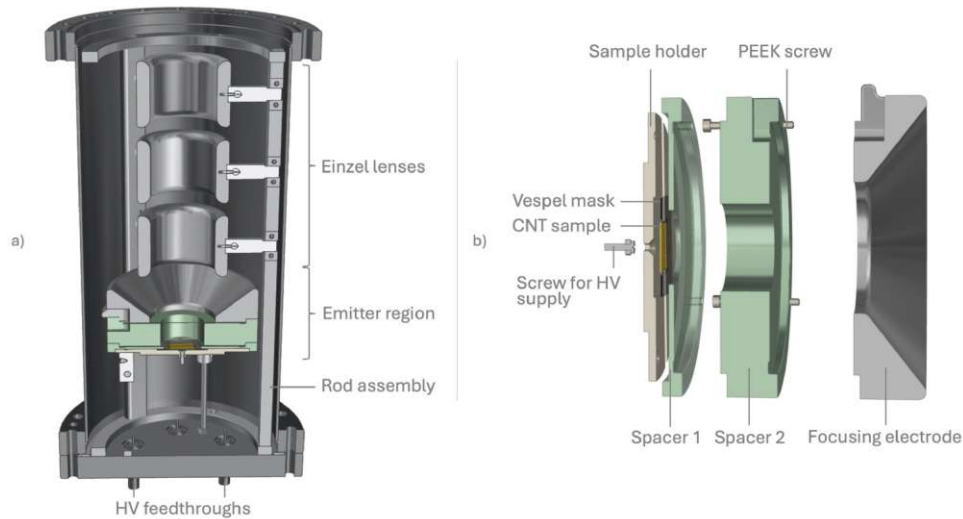


Figure 3.3: (a) Cross-sectional view of the mechanical model of the CNT-based electron gun, showing the arrangement of the Einzel lenses, emitter region and rod structure, (b) Exploded view of the emitter region, including the Vespel® mask, CNT sample, metal screw supplying high voltage, PEEK screws, two spacers and focusing electrode.

3.1.3 Einzel Lens System

Given the considerable drift distance between the sample and detector, an Einzel lens system is employed to transport and focus the beam onto an imaging screen after being released from the emitter region. Comprising of three identical, symmetrically arranged electrodes on the same axis, the Einzel lens system focuses the beam without altering the particles' kinetic energy.

Typically, the outer electrodes share a common electrical potential V_0 , while the central electrode is held at a different potential V_M . Because of its symmetrical design, the Einzel lens has identical focal distances before and after the lens. The voltage configuration determines the fringe fields and thereby influences how the particles are deflected and focused. As a charged particle passes through the lens, it encounters changing electric field strengths, causing it to be repelled or attracted to the inner side of the center electrode. The particle's trajectory is influenced by V_M , along with its incident angle, charge and energy. The Einzel lenses focusing ability depends on the design and the voltage ratio V_0/V_M .

An Einzel lens can operate in two modes, depending on the voltage ratio V_M/V_0 . In the acceleration-deceleration (A-D) mode ($V_M/V_0 < 0$), the first gap accelerates the particles, while the second gap slows them down. Conversely, in the deceleration-acceleration (D-A) mode ($V_M/V_0 > 0$), particles are first decelerated and then accelerated.

⁴Vespel® is a high-performance polyimide material [48]

The D-A mode offers a higher refractive power (shorter focal length) compared to the A-D mode. However, the A-D mode was selected for this application as it is preferable for achieving longer focal lengths with minimized spherical and chromatic aberrations [49, 50].

3.1.4 CNT samples

Various VACNT samples were produced in collaboration with the “2D Materials and Devices”-Group at the International Iberian Nanotechnology Laboratory (INL) [51]. All samples were fabricated using Plasma Enhanced Chemical Vapor Deposition (PECVD). The synthesis process begins with single-crystal silicon wafers (substrates) that are diced into different sizes and coated with a photoresist. Photolithography is then applied to define the desired pattern (e.g. hexagonal arrays). Next, the patterned substrates are coated with a 50 nm layer of aluminum oxide (Al_2O_3) to act as a diffusion barrier and a 1 nm film of iron-boron (FeB) catalyst, deposited via sputtering. Then, the photoresist is removed, leaving the catalyst layer only in the defined patterned regions.

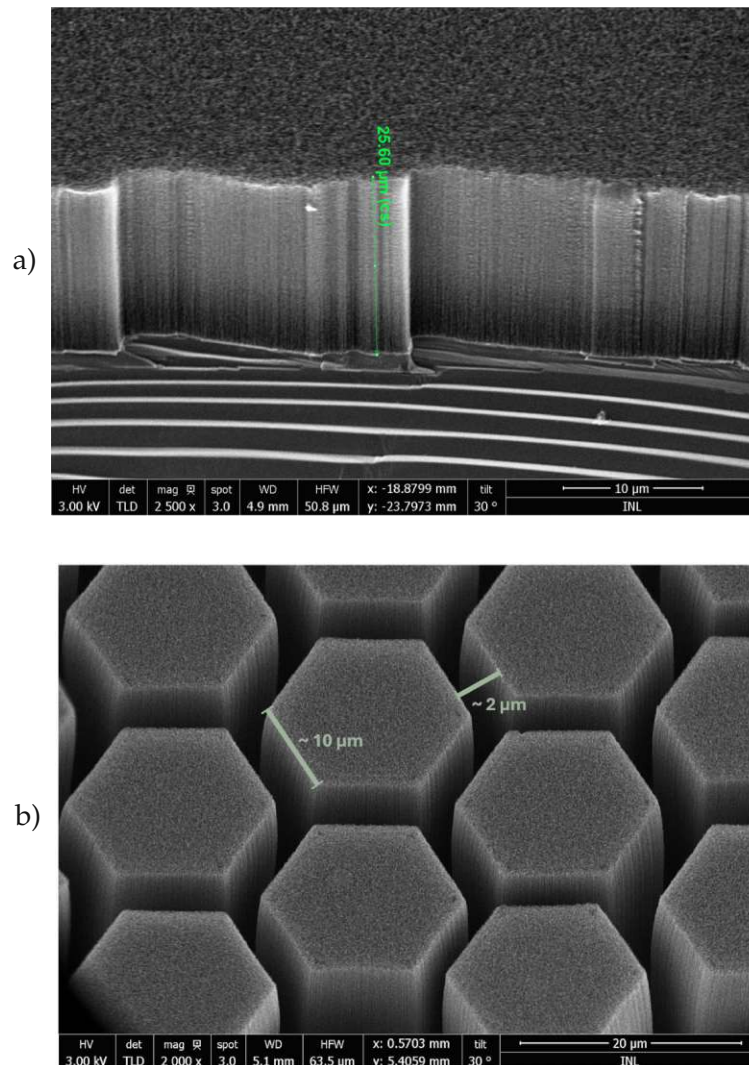


Figure 3.4: SEM images by George Machado Jr. (INL) showing (a) the height of the VACNTs from a tilted perspective, (b) the VACNTs arranged in a hexagonal pattern (10 μm side length, 2 μm gap).

The prepared substrates are placed in the Microsys 400 PECVD chamber from Roth & Rau Microsystems, where the CNT growth is initiated. The growth process involves introducing a carbon precursor gas into the chamber under carefully controlled temperature and pressure conditions, creating an environment that activates the catalyst. The vertical growth of the CNTs is facilitated, resulting in high-density, well-aligned VACNT arrays.

Post-growth, the samples are analyzed using SEM to verify the height and uniformity⁵ of the VACNT forests. The key specifications of the samples used in this project are summarized in Table 3.1, while a SEM image of the sample can be seen in Figure 3.4.

Parameter	Specification
Substrate material	Silicon (Si) wafers
Substrate size	ranging from 1 cm × 1 cm to 4 cm × 4 cm
CNT type	Vertically aligned, high-density MWNTs
CNT diameter	5 nm to 15 nm
CNT length	approx. 25 μm
Pattern type	regular hexagonal arrays
Hexagon side length	10 μm
Gap between hexagons	2 μm

Table 3.1: Summary of CNT sample requirements

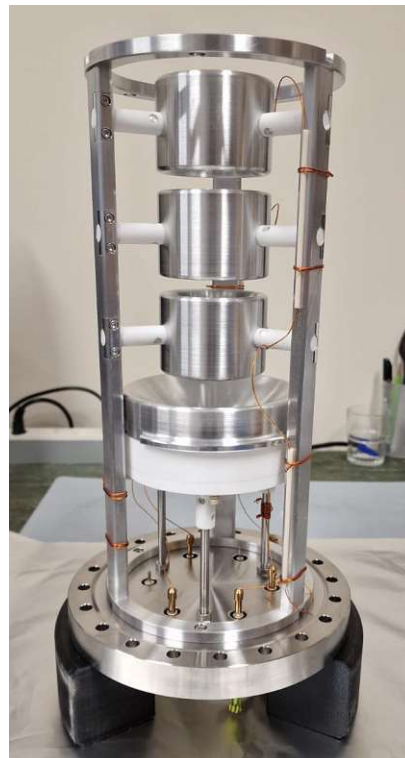


Figure 3.5: Final electron gun setup used in the experiments.

⁵Uniformity here refers to consistent height among the VACNTs across the sample.

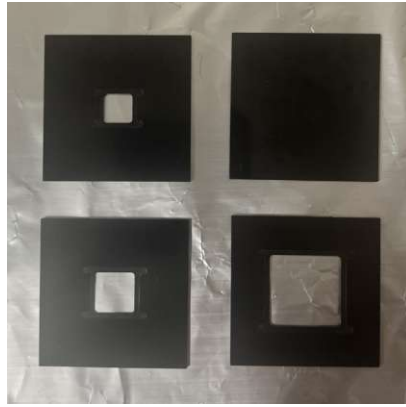


Figure 3.6: Inlays made of Vespel® (1 cm², 2 cm², 3 cm²) for different sample sizes. The top-right plate is for reference.

3.2 Testbench Set-up

3.2.1 CCTB2

In order to carry out the measurements to characterize the cold cathode electron gun, a “Cold-Cathode-Test-Bench 2” (CCTB2) was designed and built.

A photograph of the test bench setup is shown in [Figure 3.8](#). The vacuum tank (①) houses the gun assembly and includes a six-way cross for multiple connections with other instrumentation. One such connection is to an Edwards TIC Pumping Station 6i, which, along with a Pfeiffer Vacuum Dual Gauge (②), is used to maintain and monitor the UHV pressure. Current and voltage parameters are measured using a Hameg 4 3/4 digit programmable multimeter HM8012(④). High voltage for the electrodes is supplied by a ISEG THQ High Voltage Power Supply (⑤). Additionally, an ISEG HPN 120 256 High Voltage Power Supply, with a higher current limit of 25 mA, was eventually added to the setup. 33 cm downstream of the gun assembly a PHOTONICS Ion Beam Profiler (③) is placed, to visualize the beam spot. It utilizes a Microchannel Plate (MCP) [52] coupled to a phosphor screen and together with a high-resolution camera, amplifying and capturing even very dim ion beam events is possible.

The other free flange on the test bench can house another set-up called the “Cold-Cathode-Test-Bench 1” (CCTB1), which was constructed for easy and fast testing of CNT samples in previous experiments [9]. All measurements were performed at room temperature and at UHV conditions.

3.2.2 CCTB1 flange

The CCTB1 can host up to three samples, fixed in a simple diode configuration (see [Figure 3.8](#)). Each stack is composed of a stainless steel plate, where the sample is secured by a Mica [53] or a Vespel® insulating mask, allowing precise control of the emitting area. The anode, a 0.5 mm thick molybdenum plate, is grounded in order to allow for current measurements, while the cathode (the sample holder) is connected to a negative power supply to create the extracting electric field. Depending on the mask used, the cathode-anode distance can vary between 0.5 mm and 1 mm.

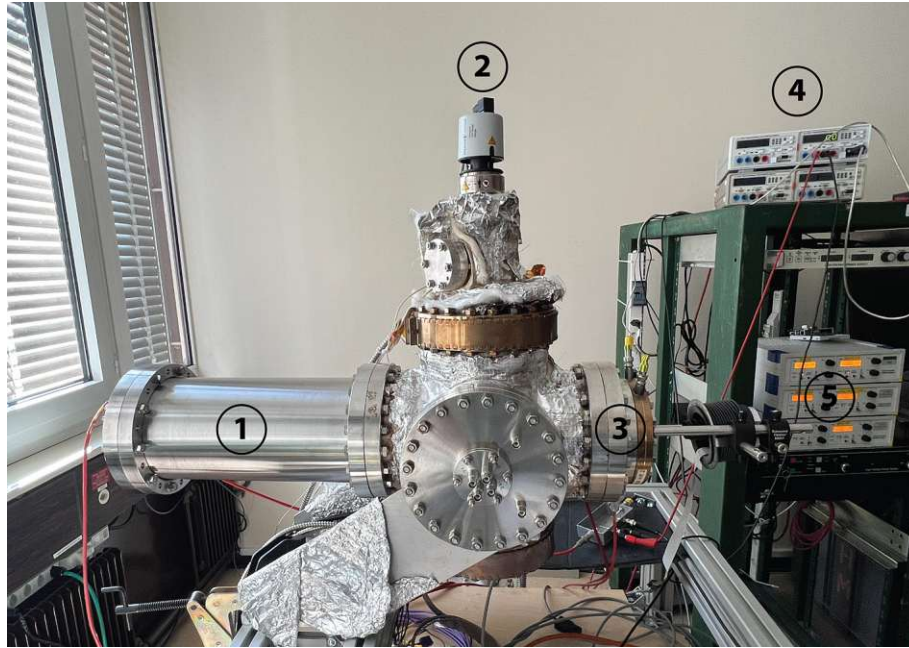


Figure 3.7: Cold-Cathode-Test-Bench 2: ① Vacuum tank with gun assembly ② Pfeiffer Vacuum Dual Gauge ③ PHOTONICS Ion Beam Profiler ④ HM6012 Multimeter ⑤ ISEG HV Power Supplies

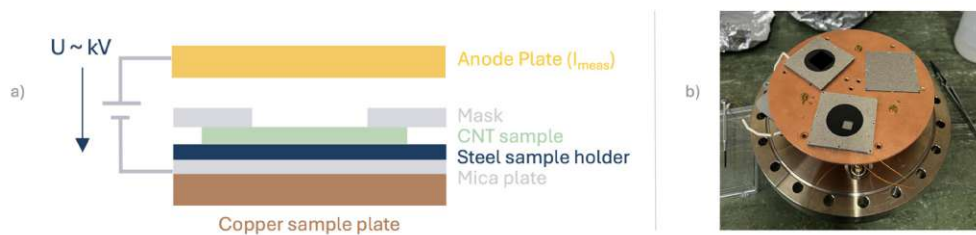


Figure 3.8: (a) Schematic of the CCTB1 sample holder stack, showing the key components: the anode plate (I_{meas}), insulating mask, CNT sample, steel sample holder and mica plate. A high voltage ($U \sim kV$) is applied across the assembly to enable electron emission from the CNT sample. (b) Top view of the CCTB1 setup, showing one mounted sample and the overall configuration

The entire stack is placed on a copper support plate on top of a mica plate for insulation between the stacks. The stacks are held together with PEEK insulating screws, except for the molybdenum plate, which is secured with ceramic screws and washers.

All electrical connections are made using copper/Kapton® wires and SHV (Safe High Voltage) coaxial feedthroughs, connecting to the various power supplies or grounded connectors with coaxial cables. During the setup, a few improvements were made compared to the original version, such as adding ceramic beads around the wires and simplifying the mounting system.

3.2.3 Data acquisition and analysis

The power supply units, the vacuum gauge and the multimeter are connected to a PC through a serial port. Data is recorded via Python scripts, allowing for real-time monitoring of pressure and current values from the multimeter and

gauge. A separate script is used to control ramp-up of the high-voltage power supplies, where the start and end voltage as well as the step size and duration can be set manually. The acquired data is then plotted, fitted and analyzed using several Python scripts.

3.3 Microscopic analysis

Different microscopic analyses were performed in collaboration with the EN-MME-MM section at CERN and INL:

- **Scanning Electron Microscopy (SEM):** The SEM study was performed at INL using an FEI Quanta 650 FEG Environmental SEM.
- **Optical analysis:** A Keyence VHX 970F optical microscope was used to optically analyze the grid.

4 Simulation Study

4.1 Simulation Overview

The main objective of this simulation study was to predict the electron beam behavior during full-scale operation and to ensure the internal consistency of the results. The simulations were performed using COMSOL Multiphysics® [54] and CST Studio Suite® (CST) [55]. Both programs use finite element methods to solve the Maxwell equations, simulating the behavior of charged particles in electromagnetic environments.

Simulating the setup and finding the right balance between accuracy and computational resources was a challenging task. In particular, the grid introduced several complexities. Due to the rectangular grid structure, cylindrical symmetry is not applicable, so that three-dimensional simulations became necessary. In addition, each 3 μm thick wall must be represented by a minimum of two mesh cells to ensure precise particle tracking. Furthermore, the number of mesh cells is correlated to the simulation time and is limited by the available computing power. Since the grid contains about 4.9×10^6 holes, a high number of mesh cells were required, which lead to a significant computational effort.

4.1.1 Simulation Strategy

To manage this complexity, several strategies were applied. First, a simplified model of the gun was created directly within the simulation software instead of importing detailed CAD¹ models intended for manufacturing. This allowed for freedom in the design process while reducing the complexity of the global mesh and the computational load.

In addition, the electron gun was simulated at different scales of its full size, which reduced the total number of grid cells required. Comparing the results at different scales also helped to verify that the simulation setup correctly represents the physical system.

Each simulation was further divided into two stages:

- **Stage 1:** Simulation of the electron source and initial beam generation.
- **Stage 2:** Simulation of beam transport through the Einzel lenses.

Stage 1 was performed with the Particle Tracking Solver in the CST Studio Suite and the resulting beam profile was analyzed. In the second stage, the beam properties were reconstructed in COMSOL using a full-size model. Several reasons led to the decision to use both CST and COMSOL. CST is fast and has many built-in post-processing options, yet it lacks specific fine-tuning options that are available in COMSOL. The combination of the strengths of both tools allowed for a streamlined representation of the behavior of a CNT sample in the physical test bench setup.

¹Computer-Aided Design

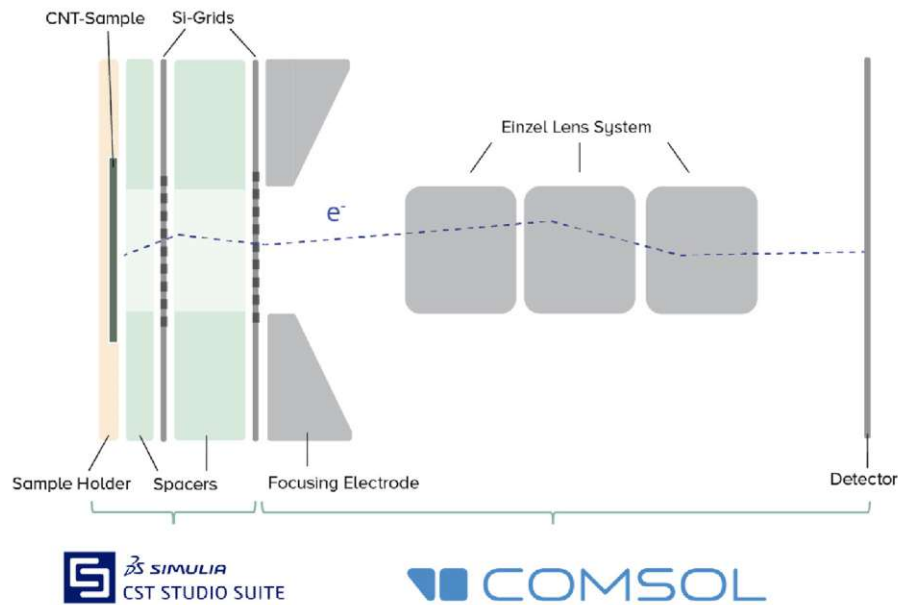


Figure 4.1: Illustration of simulation layout

4.2 CST Simulations (Stage 1)

Several simulation setups were considered, tested and refined before the final layout was found. A key focus of the simulation setup in stage 1 was to ensure straight field lines near both grids. This is necessary to minimize the transverse momentum transferred to particles as they pass through the grid.

As mentioned above, a simplified geometry was used to avoid complex meshes that could cause numerical errors or instabilities in the solver. The gun was scaled to 1%, 2% and 3% of its original size in the transversal (in x - and y -direction) plane. The dimensions used for each scaled simulation is summarized in Table 4.1. When scaling the geometry, the electric field strength must also be taken into account. If the gun was scaled longitudinally (in the z direction), the voltages applied to the cathode and grid would have to be adjusted to ensure a constant field strength. By scaling only in the transverse direction, this adaptation is avoided, while still maintaining the most important physical properties and keeping the beam distance in the z direction the same during the rescaling in stage 2.

The focusing electrode's primary function is to keep the field lines straight, which can be archived by using periodic boundaries in the transverse plane. These boundaries link the edges of the simulation domain, thus recreate the electromagnetic fields at the edges. In this way, the simulation can be executed on a small section of the grid, while the periodic boundaries emulate the behavior of a fully extended grid in the $x - y$ plane. This approach further optimizes the simulation and minimizes computational costs.

4.2.1 Simulation Configuration

Mesh

Global and local mesh properties were carefully selected to maintain the required precision without unnecessarily increasing the simulation time. Finer steps were used near critical areas with high field variations. Near the grid, the step width in the x , y and z directions is $1.2\ \mu\text{m}$, with a z -extension of $0.05\ \text{mm}$. Near the cathode, a coarser step width of $3\ \mu\text{m}$ is applied, along with the same z -extension.

Particle Emission Model

For all simulations, the CNT internal field-induced emission model was used with a circular source type. The following parameters were set based on previous studies [9]: the initial kinetic energy $E = 0.1\ \text{eV}$, two Fowler-Nordheim equation-related material-specific constants $a = 3.1537 \times 10^{-11}$ and $b = 7.5793 \times 10^6$ and the angle spread $\alpha = 89^\circ$. The potentials were set according to the requirements: the CNT sample is fixed to $-355\ \text{V}$ while the first grid is at $4000\ \text{V}$ and all other components are grounded.

Geometry Adaptations

The inner diameter of the spacers limits the grid area where the beam can expand anyways, therefore the meshed region was designed as a circle. To ensure smooth boundary conditions, the circular grid was enclosed within a rectangular frame, as the boundary box in CST is always rectangular. The spacers were modeled as rings, while the thickness of the sample holder was kept thin to minimize solver artifacts at the edges.

4.2.2 Parameter Monitoring and Post-Processing for COMSOL

Four key parameters — Beam Divergence Angle, Mean Energy, Emittance, Maximum Transversal Position and Transparency² — were tracked during each simulation to obtain an overview of the beam's characteristics before exiting the focusing electrode.

These parameters were recorded by 2D Particle Beam Monitors positioned perpendicular to the beam's direction of travel (in the z -plane), collecting data from all particles passing through the monitor plane.

After the simulations were carried out, post-processing was done in CST and with Python scripts. In particular, the "Observable As Histogram" function, where the orbital angle spread can be plotted as a histogram, was used. The results of the beam analysis was then used to generate the initial beam profile in COMSOL.

²Transparency in this context refers to the percentage of particles that pass through the gun without being absorbed or deflected.

Parameter	Real Size	1% Scale	2% Scale	3% Scale
Size of CNT sample	40 mm × 40 mm	0.3 mm	0.6 mm	1.2 mm
Thickness of sample holder	3 mm	0.02 mm		
Diameter of sample holder, spacers and grids	120 mm	1.2 mm	2.4 mm	4.8 mm
Inner diameter of spacer 1 / spacer 2	30 mm / 35 mm	0.3 mm / 0.35 mm	0.6 mm / 0.7 mm	0.9 mm / 1.05 mm
Thickness of spacer 1 / spacer 2	1.5 mm / 19.75 mm	Not Scaled		
Thickness of grid 1 / grid 2	0.05 mm	Not Scaled		
Size of meshed grid area	30 mm × 30 mm	∅ 0.3 mm	∅ 0.6 mm	∅ 1.2 mm

Table 4.1: Comparison of simulation parameters for different scales

4.3 COMSOL Simulations (Stage 2)

Proceeding to the second phase of the study, the objective was to simulate the transport and spot size of a real-size beam through the focusing electrode and the Einzel lenses. The previously obtained maximal orbital angle was incorporated into COMSOL for the generation of a beam that could be transported through the Einzel lenses.

Similarly to stage 1, some geometry was simplified to avoid boundary issues in the solver. A round beam inlet with the specified electron beam properties is placed at the simulation origin, which corresponds to 148 mm downstream of the flange (55 mm downstream of the source). The surrounding model geometry consists of the focusing electrode, the Einzel lenses and a round beam inlet. The focusing electrode and the outer lenses were set to ground, only the inner lens voltage V_M was parameterized. A summary of the parameters used in the simulation can be found in [Table 4.2](#) [56].

In this set-up, two studies are necessary: first is a stationary study, used to calculate the electric potential. Then, the resulting electric field is applied to the model electrons via the Electric Force feature. Finally, a time dependent study is carried out to simulate the particle trajectories over time. For post-processing various 3D and 2D plot options were used to visualize the electric field and the particle trajectories for different V_M .

4.3.1 Simulation Configuration

Mesh

A predefined fine mesh setting was used near the lens cylinders, to allow for precise solving of the electric field in the gaps between them. For the other elements, a coarser predefined mesh was applied to save on simulation time.

Particle Emission Model

The particle beam was generated with an uniform release time distribution. KV³ sampling from the phase space ellipse was chosen with an upright orientation. The initial transverse velocity was set with a maximum transverse displacement and a maximum transverse (orbital) angle obtained from step 1. The longitudinal velocity was determined by setting a constant kinetic energy E_0 .

Table 4.2: Parameters used in the COMSOL simulation. The value of $\bar{\sigma}_m$ can be found in [subsection 5.1.3](#).

Parameter	Value	Units	Description
V_0	parameterized	V	Voltage on inner cylinder
E_0	355	eV	Kinetic energy of particles
T	1.3423×10^{-7}	s	Time to reach end with no force
L_{vac}	59.2	cm	Width of vacuum chamber
R_{vac}	7.95	cm	Height of vacuum chamber
L_{cyl}	5	cm	Length of cylinders in lens
T_{cyl}	1	cm	Thickness of cylinders in lens
R_{cyl}	2.5	cm	Radius of cylinders
d_{lens}	3.65	cm	Downstream distance of start of lens
cyl_{sep}	1	cm	Separation of cylinders
x_m	1.75	cm	Maximum transverse displacement
x'_m	$\bar{\sigma}_m$	rad	Maximum transverse orbital angle

³In 3 dimensional phase space, the KV distribution particles are positioned uniformly across the beam cross-section, with roughly equal distances between the particles [17].

5 Simulation Results

5.1 Stage 1

This section summarizes the results of the initial simulation stage carried out in CST.

5.1.1 Beam Characteristics

Figure 5.1 and Figure 5.2 show a comparison of five beam parameters (Beam Divergence Angle, Mean Energy, Emittance, Maximum Transversal Position and Transparency) measured across three different simulation scales (1%, 2% and 3%). The abscissa represents the values obtained from each beam position monitor that was set up, tracking the properties of the beam along its direction of motion.

The mean beam divergence angles are 6.09×10^{-4} rad, 6.33×10^{-4} rad and 6.40×10^{-4} rad for the 1%, 2% and 3% scales, respectively, with an overall mean of approximately 6.27×10^{-4} rad. The error ranges, representing the difference between the minimum and maximum beam divergence values are: 4.93×10^{-4} rad for 1%, 4.30×10^{-4} rad for 2% and 4.07×10^{-4} rad for 3% scale.

The final averaged emittance calculated as the mean of the three scaled is 1.182×10^{-3} mm · rad. The exiting radius is 0.173, 0.342 and 0.521 for the 1%, 2% and 3% simulations, respectively.

5.1.2 Electric Field and Particle Trajectories

Figure 5.3a illustrates the electric field distribution within the electron gun, while Figure 5.3c shows the equipotential lines near the grid structure. An example of particle trajectories can be viewed in Figure 5.3b.

5.1.3 Maximal Orbital Angle

Table 5.1 summarizes the calculated maximal orbital angles in the transverse plane of the beam after passing through grid 2. The mean values for each coordinate are $\bar{\sigma}_x = 0.0224$ rad and $\bar{\sigma}_y = 0.022$ rad. The maximum transverse angle, $\bar{\sigma}_m = 0.022$ rad, was used as an input parameter to generate the beam in COMSOL (see Table 4.2).

Table 5.1: Maximum Orbital Angle extracted from differently scaled CST simulations

Simulation Scale	σ_x [rad]	σ_y [rad]
1%	0.0222	0.0219
2%	0.0223	0.0222
3%	0.0228	0.0222

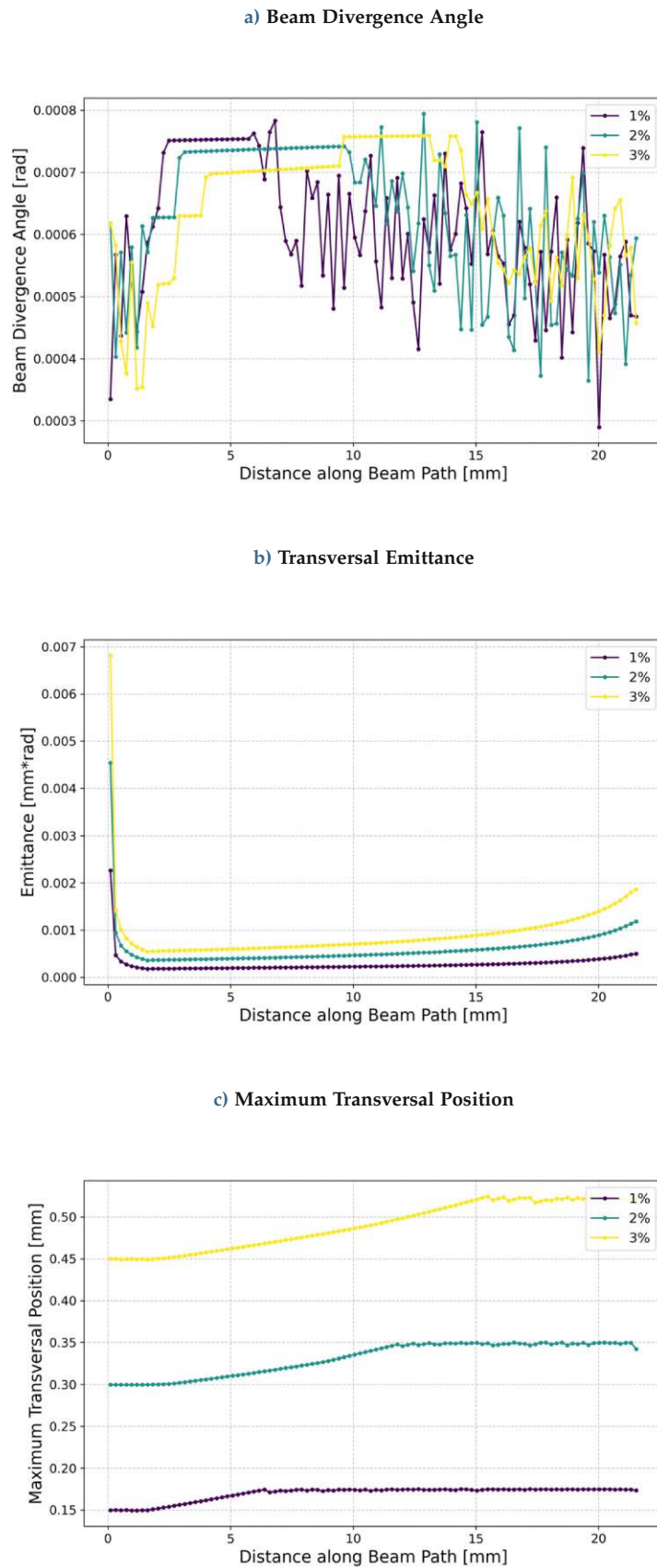


Figure 5.1: Comparison of the Beam Divergence Angle, Emittance x and Maximum Transversal Position over the distance along the beam path

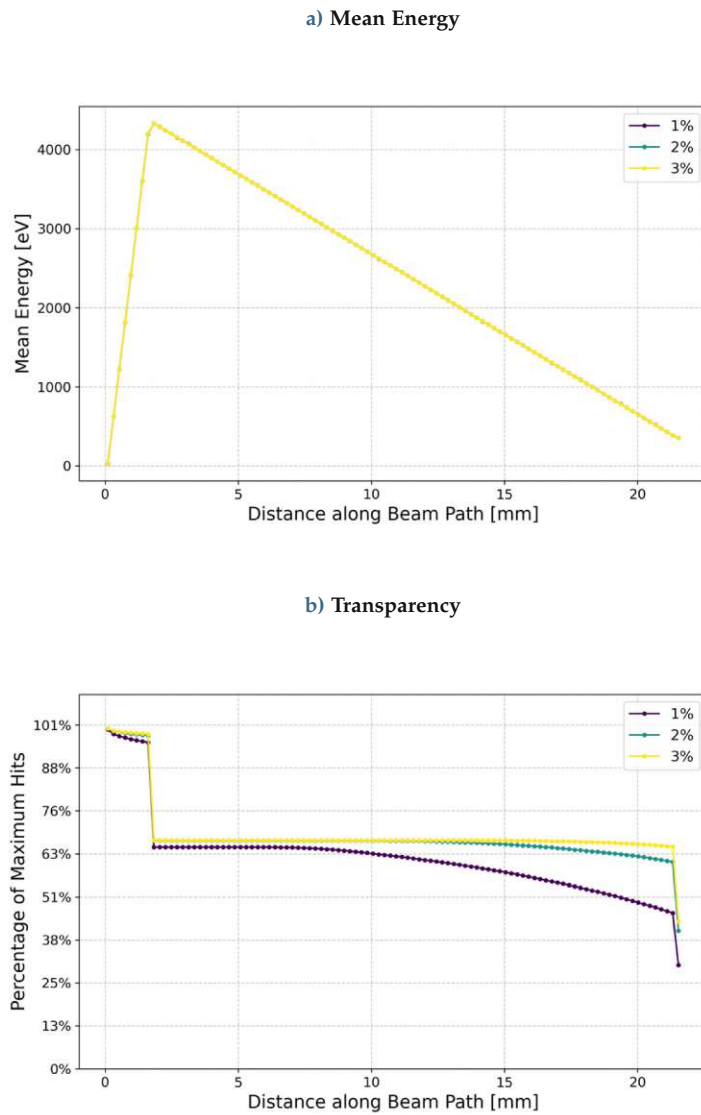


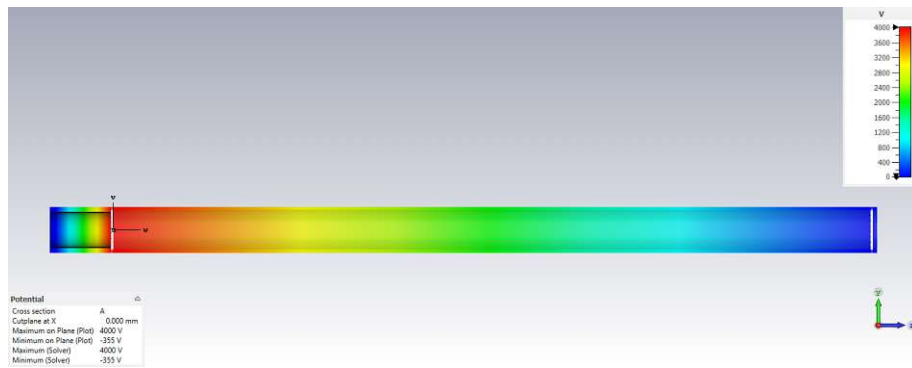
Figure 5.2: Comparison of the Mean Energy and the Transparency over the distance along the beam path

5.2 Stage 2

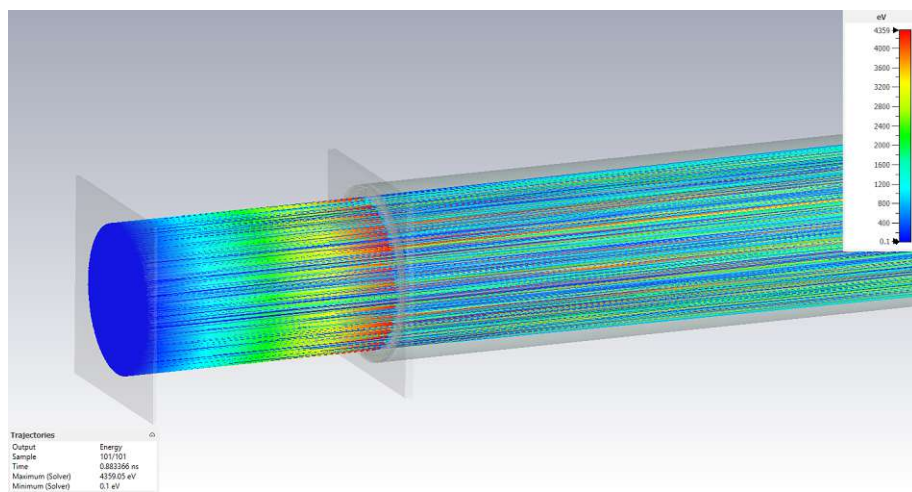
The following section outlines the results obtained from the COMSOL simulation of the particle trajectories through the Einzel lenses.

5.2.1 Electric Field and Particle Trajectories

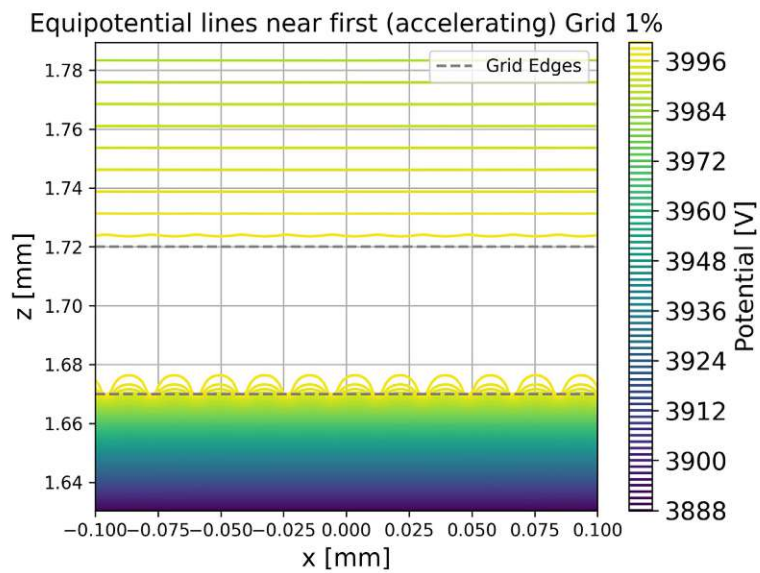
A cross-section of the equipotential surfaces near the Einzel lenses are shown in Figure 5.4a for a middle lens voltage of 50 V. Figure 5.4b illustrates one of the simulated beam trajectories, where the color represents the particle kinetic energy in SI units.



a) Electric potential along the beam path



b) Particle trajectories



c) Equipotential lines near the first grid

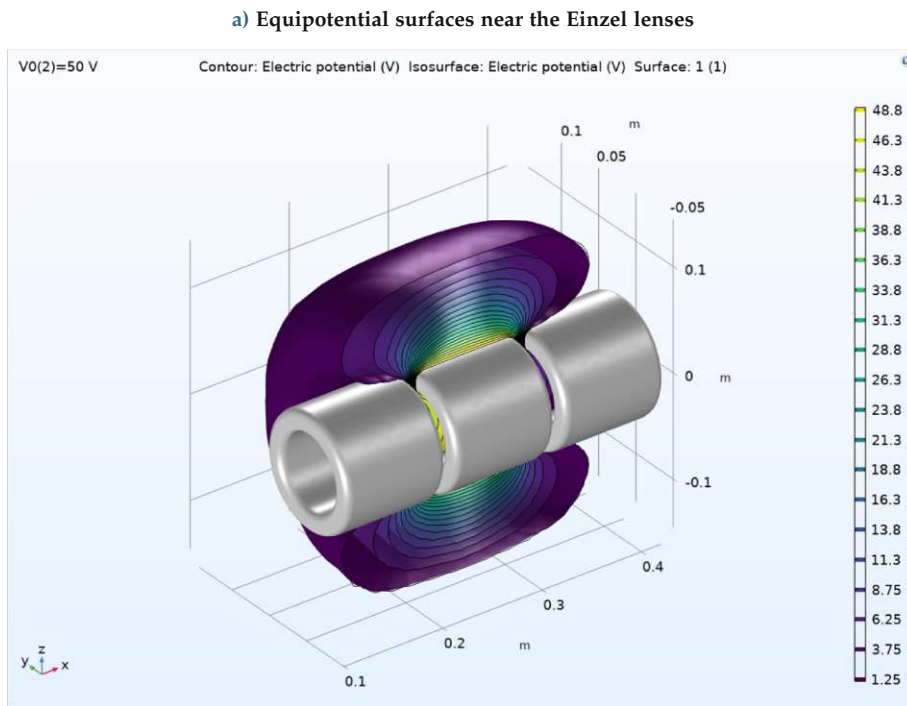
Figure 5.3: Illustrations showing (a) electric potential distribution, (b) particle trajectories and (c) equipotential lines near the first grid.

Table 5.2: Beam Radius and Area at different middle lens voltages

V_M [V]	Radius [mm]	Area [mm ²]
0	21.82	1484
50	21.56	1373
100	20.05	1120
355	17.92	592
400	22.4	958
500	32.97	2161

5.2.2 Beam Profile

The beam profiles at the detector distance for different middle lens voltages are shown in [Figure 5.5a](#), while their overlapped outlines are displayed in [Figure 5.5b](#). The beam surface area and the estimated beam radius for each profile are summarized in [Table 5.2](#).



b) Beam Trajectories for $V_M = 355$ V

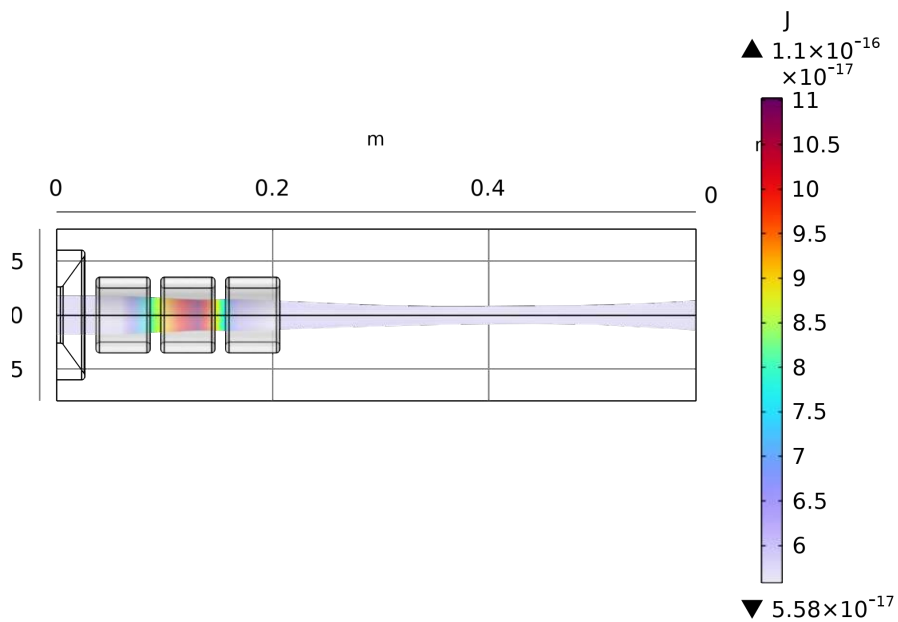


Figure 5.4: Beam trajectory and equipotential surfaces in COMSOL

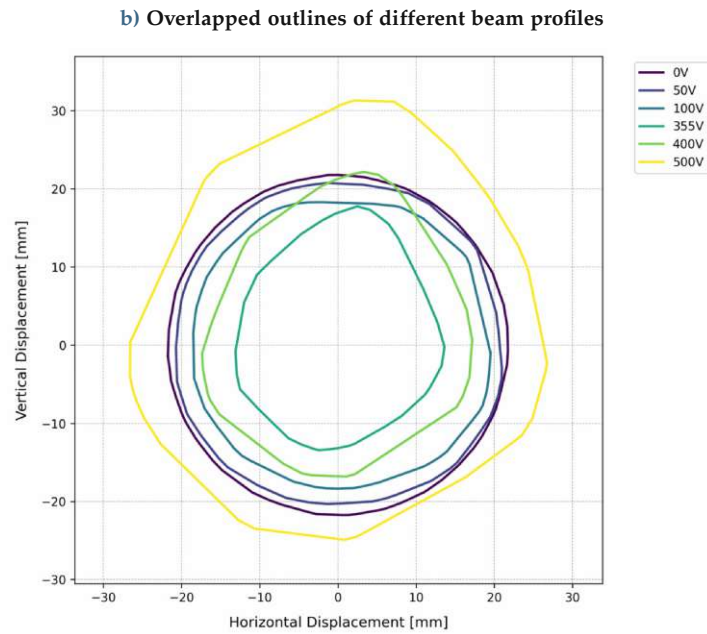
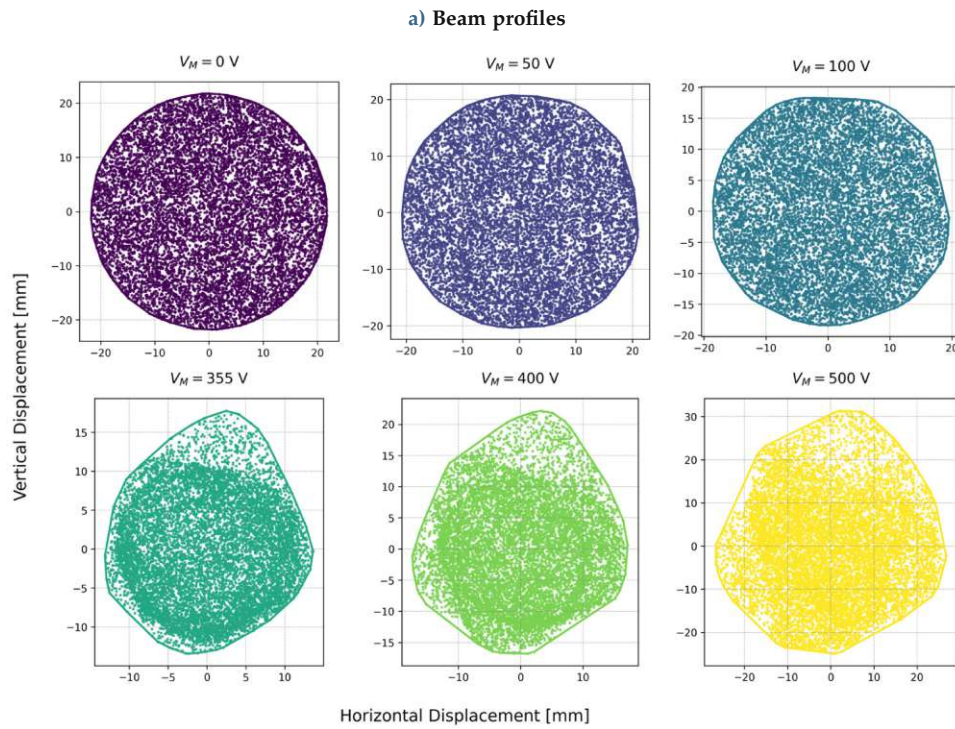


Figure 5.5: Beam shapes at detector distance for various applied voltages V_M



Die approbierte gedruckte Originalversion dieser Diplomarbeit ist an der TU Wien Bibliothek verfügbar
The approved original version of this thesis is available in print at TU Wien Bibliothek.

6 Experimental Results

6.1 Field Emission Performance CCTB1

This chapter reports the experimental results.

6.1.1 Conditioning, Lifetime and Long-term Stability of VACNTs

Figure 6.1a shows an example of a ramp-up process for a $2 \times 2 \text{ cm}^2$ sample, where both the current density and pressure are plotted against time. The voltage on the anode was continuously increased in small voltage steps. The first ramp-ups displayed a large amount of current spikes with a high amplitude. However with more runs, more stable datasets were obtained.

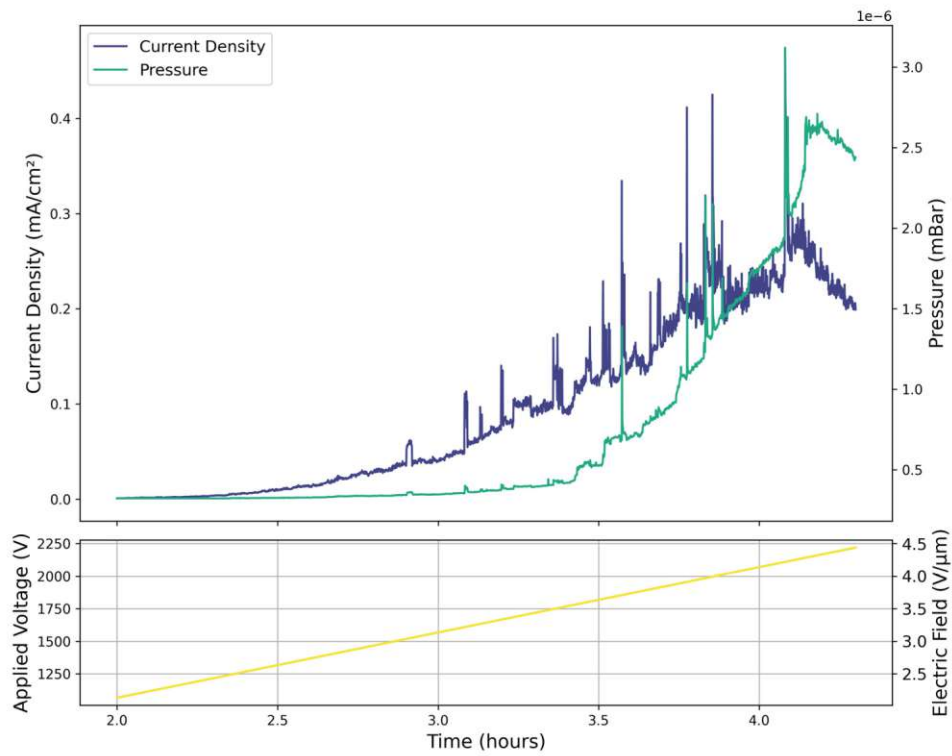
6.1.2 Characterization and Field Emission Properties

Two different samples ($2 \times 2 \text{ cm}^2$ and $4 \times 4 \text{ cm}^2$) were evaluated. For the $4 \times 4 \text{ cm}^2$ consecutive ramp-up were performed, resulting in three different datasets (*I1*, *I2* and *I3*). In contrast, dataset *J* and the two measurements for the $2 \times 2 \text{ cm}^2$ sample were done independently. Their characteristic field emission properties, such as the turn-on field (E_{on}) and threshold field ($E_{\text{threshold}}$) at 0.01 mA/cm^2 and 0.1 mA/cm^2 respectively, are summarized in Table 6.1. The obtained current density curves are displayed in Figure 6.2a and Figure 6.2a.

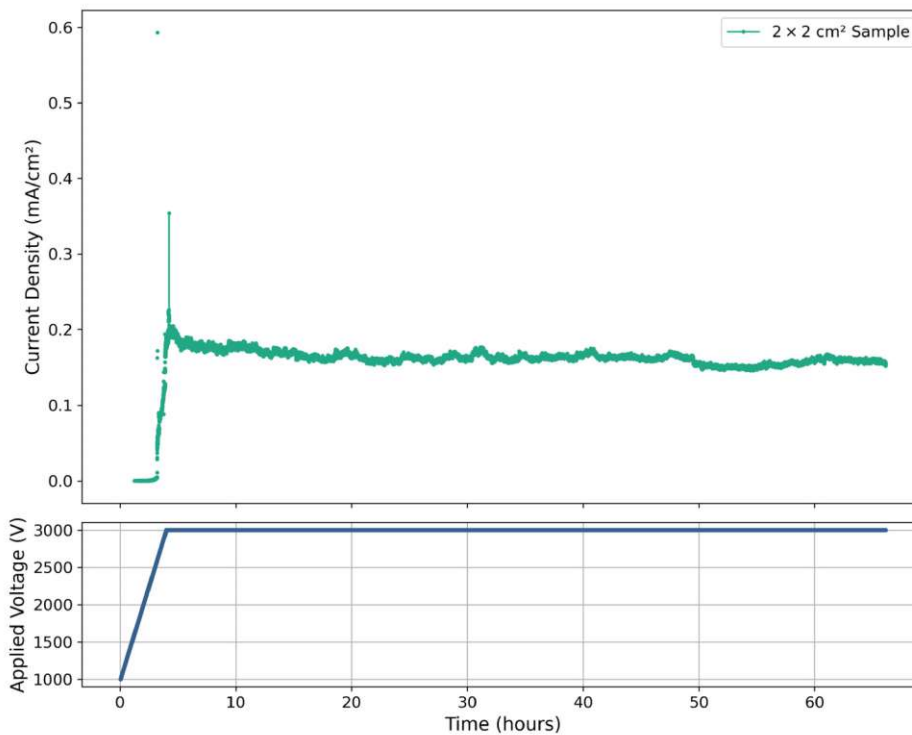
Table 6.1: Turn-on field (E_{on}) and threshold field ($E_{\text{threshold}}$) at 0.01 mA/cm^2 and 0.1 mA/cm^2 for different datasets

Dataset	E_{on} [V/ μm]	$E_{\text{threshold}}$ [V/ μm]
4x4 I1	1.45	-
4x4 I2	1.50	1.61
4x4 I3	1.51	-
4x4 J	1.72	2.90
2x2 A	2.65	3.34
2x2 B	4.73	5.19

a) Current density, pressure, applied voltage and electric field



b) Current density stability

Figure 6.1: Ramp-up and stability measurement for sample $2 \times 2 \text{ cm}^2$ performed on CCTB1.

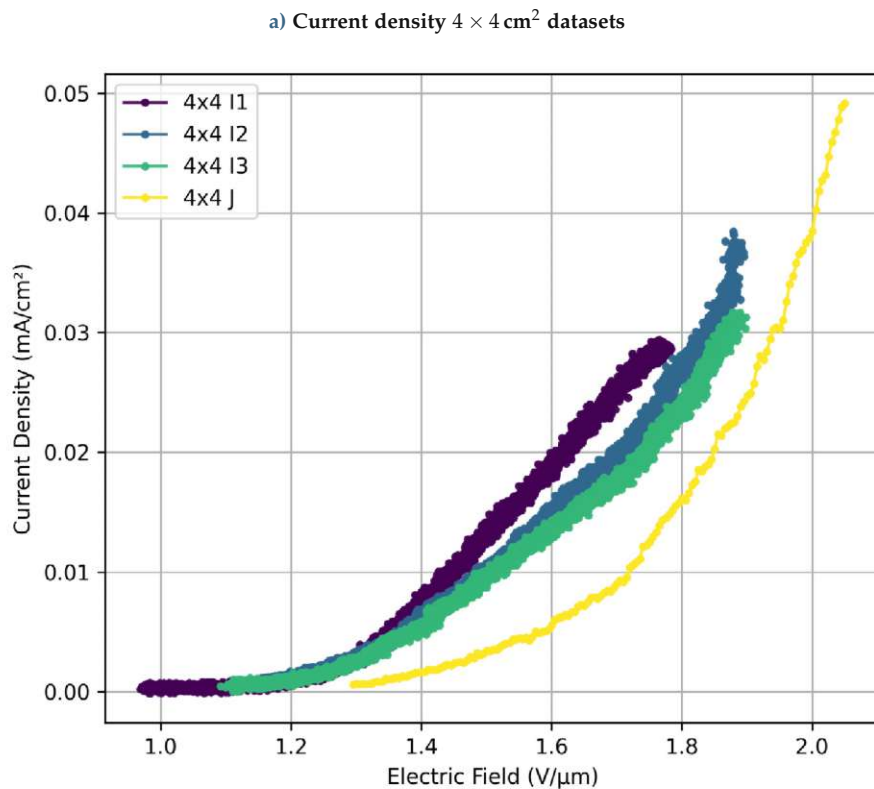
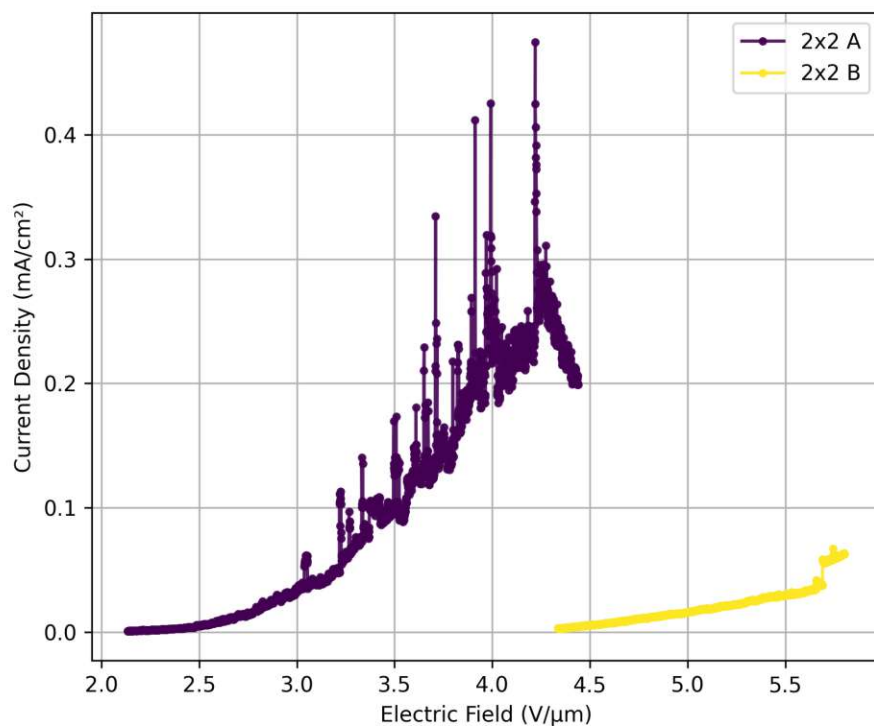
b) Current density for $2 \times 2 \text{ cm}^2$ datasets

Figure 6.2: Current density for different samples sizes

6.1.3 Fowler–Nordheim plot analysis

Fitting the current density curves to Equation 2.6, a Fowler-Nordheim plot Figure 6.3a can be obtained. The corresponding fit results and estimations for

the field enhancement factor and the emitter radius are summarized in Table 6.2. Another visualization, the Seppen-Katamuki plot, derived from the slope and intercept of the Fowler-Nordheim plot, is shown in Figure 6.3b.

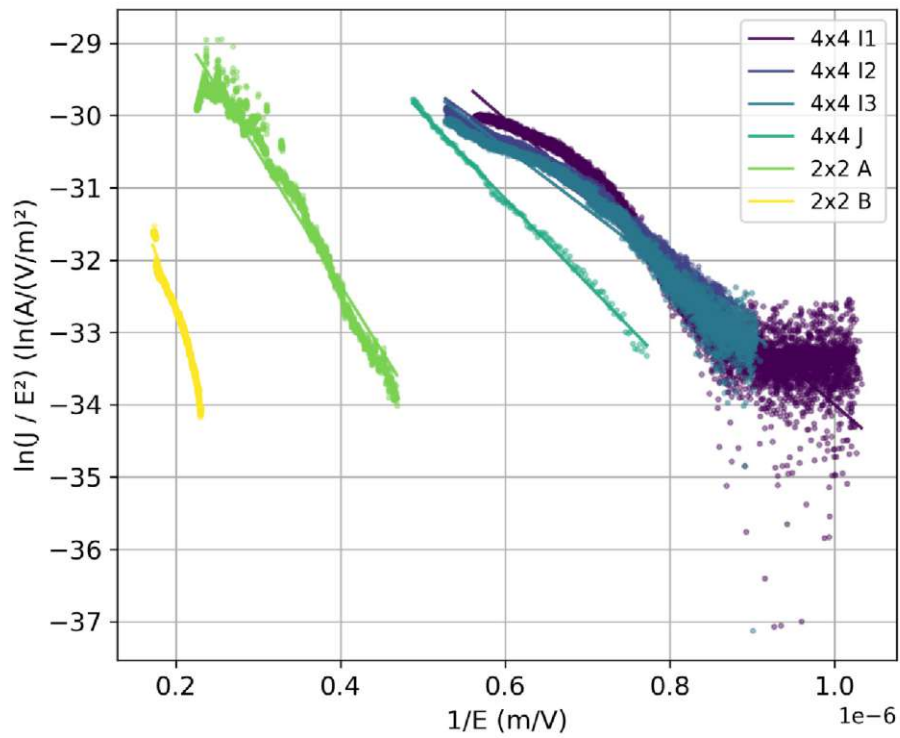
Table 6.2: Fitting parameters for different datasets.

Dataset	Slope	Intercept	R ²	β (nm ⁻¹)	Radius (μ m)
4x4 I1	-9.87×10^6	-24.13	0.940	6.61×10^{-6}	30.27
4x4 I2	-8.07×10^6	-25.51	0.968	8.08×10^{-6}	24.75
4x4 I3	-8.60×10^6	-25.28	0.956	7.58×10^{-6}	26.39
4x4 J	-1.18×10^7	-24.09	0.996	5.54×10^{-6}	36.11
2x2 A	-1.82×10^7	-25.06	0.962	3.58×10^{-6}	55.86
2x2 B	-3.45×10^7	-25.85	0.958	1.89×10^{-6}	105.80

6.2 Electron Beam Profile CCTB2

Figure 6.4 shows images of the captured beam on the phosphor screen connected to the MCP plate, using a $4 \times 4, \text{cm}^2$ sample that was mounted in the sample holder as previously explained. The diameter of the screen is 8 cm and the images are taken one second apart each other. It was observed that fluctuations in brightness correlate with an increase in the current on the grid.

a) Fowler-Nordheim plot



b) Seppen-Katamuki plot

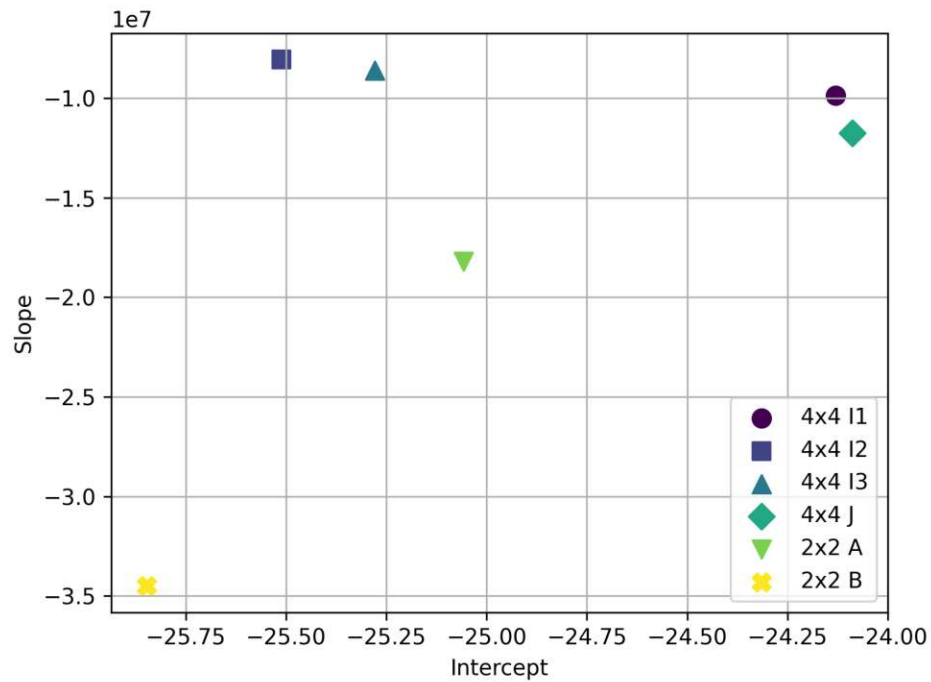
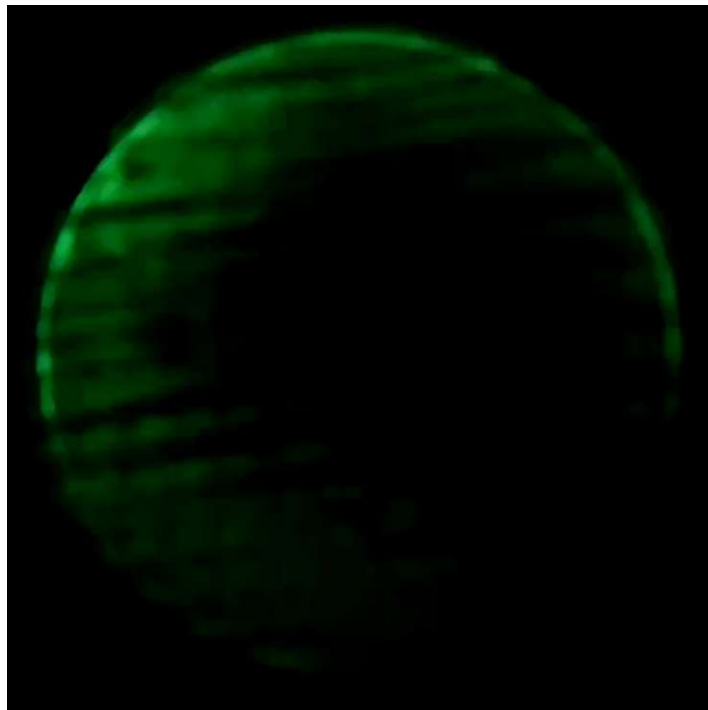


Figure 6.3: Fowler-Nordheim analysis

a) $t = 0\text{s}$



b) $t = 1\text{s}$

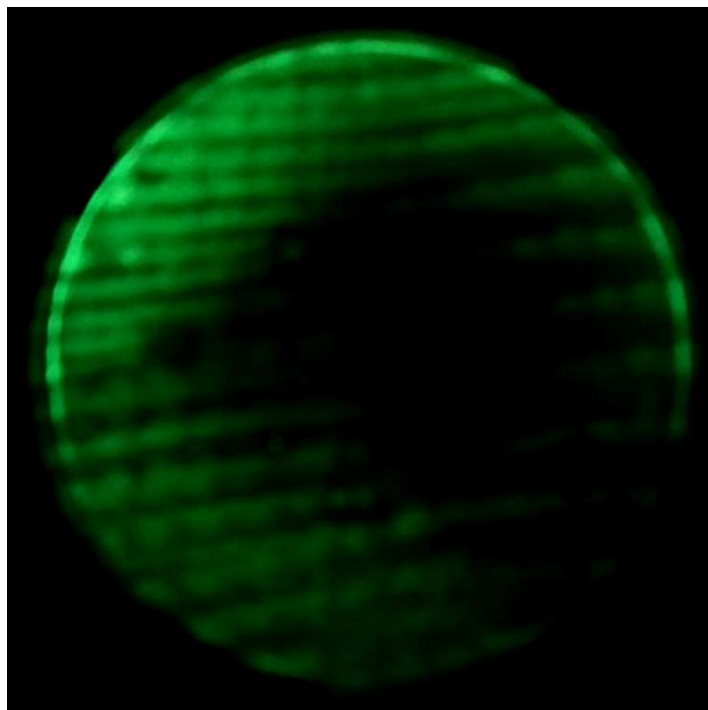


Figure 6.4: Images of the beam spot on the phosphor screen

7 Discussion

7.1 Simulation

7.1.1 Stage 1

The interpretations of the beam parameters obtained in stage 1 are summarized in the following paragraphs.

- **Beam Divergence Angle (see Figure 5.1a):** The beam divergence angle curves are relatively consistent across all simulations, showing only minor fluctuations. The error ranges are relatively low.
- **Mean Energy (see Figure 5.2a):** The mean energy is uniform across all simulations, as expected when applying similar potentials. Initially, the particles gain energy when they are accelerated towards the first grid, but then lose energy as they are defocused by the second grid.
- **Emittance (see Figure 5.1b):** The transversal emittance behavior is consistent across all curves. The visible offset can be explained by the radius dependence of ϵ . First, the emittance decreases as the beam travels through the first grid, indicating that the beam is being focused, which reduces the spread of particle trajectories. The final emittance as a mean over all scales is relatively low when exiting the second spacer, indicating a well focused beam.
- **Maximum Transversal Position (see Figure 5.1c):** The offset in the beam's maximum transversal position, effectively the beam's envelope, is clearly visible, as anticipated when scaling linearly. It can be observed that as the beam passes through the two drift tubes, it expands. It is clear that the particles have the same speed but have more room to travel before being limited by the spacer walls. The larger the simulation, the greater the radius of the spacer, allowing the particles more space to expand, resulting in a longer linear slope.
- The exiting radius is in good accordance with the dimensions of the respective inner radius of the second spacer (see Table 4.1) and a low emittance beam.
- **Transparency (see Figure 5.2b):** All simulations begin with the same number of particles, but as the beam progresses, the percentage of hits declines. This is expected, as the electrons hit the edges of the spacer and are absorbed there. A drop to around 60% is observed for all scales after passing the first spacer. This is in accordance with the expected transparency of 30-40% per grid, as indicated in previous simulations by Galante [9].
- Interestingly, the 1% scaled simulation loses the most particles during the second drift tube, likely due to its smaller transverse size relative to the beam path, leading to a greater impact from the tube edges. The 3% scaled simulation performs best with 43.3% transparency, retaining more particles and aligning more closely with the expected behavior of a fully scaled gun.

- The Maximum Orbital Angle is relatively small and similar across all scales and in both the x - and y -plane, again aligning with the obtained emittance.

The electric field is an important factor in the design of the electron gun, as it directly affects particle acceleration, focusing and beam divergence. As said before, it is generated by the applied voltages on the cathode, grids and anode. The field lines (see [Figure 5.3a](#)) are straight and uniform, with the highest field near the cathode, gradually decreasing towards the anode. Showing no significant field disturbances or boundary errors, this indicates that the mesh size was sufficiently small to ensure precision.

One of the primary objectives in the simulation setup for stage 1 was to achieve straight field lines before the grid in such a way that the beam remains focused and stable as it travels through the electron gun.

When plotting the isolines, or equipotential lines, near the grid (see [Figure 5.4a](#)), it is clear that the grid structure has a significant impact on the electric potential. The field penetrates partly into the grid structures, as visible in the rounded isolines. Notably, after passing the grid, the isolines quickly return to being straight within just a few microns, indicating that the grid does not introduce a transverse kick to the particles.

Overall, the simulations show that the beam is stable across all three simulation scales. The beam diameter grows as expected with larger geometries and the transparency values align with previous studies. The observed maximum orbital angle and the emittance is relatively small, indicating a converged beam that can be focused well in step 2. These results suggest that the applied scaling approach is feasible and internal consistency can be assumed.

7.1.2 Stage 2

The COMSOL simulation shows that the beam remains stable. The lenses focusing behavior can be observed as expected when different voltages are applied. The input beam, constructed according to the specified parameters, exhibits a low divergence.

The energy remains the same before and after passing through the lens, as shown in [Figure 5.5](#), which is essential for optimal Einzel lens performance. Overall, the results indicate a clear dependence of beam shape on the applied voltage (see [Figure 5.5a](#)).

At $V_M = 0$ V, the beam is relatively large and displays a circular outline, with the particles evenly distributed across the beam's surface. As the voltage is increased, more asymmetric distortions both in the beam outline and the particle distribution appear. These shape distortions in the beam spot roundness can be attributed to an increased focusing and lens aberrations, causing a poorly focused beam. The beam at $V_M = 355$ V demonstrates the smallest surface area of 592 mm^2 , suggesting optimal focusing at this voltage. Beyond $V_M = 355$ V, the beam size increases again. This is due to over-focusing, where the focal plane (the point where the beam envelope converges) is too close to the exit of the final Einzel lens. As a result, the beam starts to diverge again after passing through this focal point, leading to an expanded beam shape at the detector.

7.2 Experimental Data

7.2.1 Field Emission Performance CCTB1

From the experimental data obtained from different VACNT samples in CCTB1 (see subsection 6.1.2), a few key observations can be made. Firstly, unstable currents with high current spikes for the first few sweeps were observed. Such abrupt drops are visible in Figure 6.1a. However, with more sweeps, fewer outliers were observed, which aligns with reports in the literature [1]. Even for VACNT, which already exhibit high uniformity compared to other CNT-based sources, small differences in the CNT height can cause significant problems [2]. The observed current spikes are probably caused by protruding tips that are being “burnt off.” As a higher CNT height is correlated with higher current, the over-emission induces Joule heating, which in turn can cause tip deformation. It has been shown that after a few “conditioning” sweeps, the most dominant CNTs and any residual gas adsorbates on the surface are removed, allowing for a more stable current [1, 5].

It is also important to note that for all samples, much less current was observed than expected. Based on past research by Galante, current densities up to 2 mA cm^{-2} were anticipated, in stark contrast to the values reported here, which are lower by approximately one to two orders of magnitude [9].

Various hypotheses can be proposed to explain these underlying problems. One assumption is poor adhesion between the substrate and the CNT. At high current densities, the CNT can easily detach when the adhesion force is too small [2]. Another hypothesis is that the alumina layer used in the CVD process is negatively influencing electrical contact. Although a thin alumina layer is commonly used in producing CNT emitters, a layer that is too thick or unevenly distributed could create an insulating barrier in some areas of the sample. Another idea is that too many CNTs degrade over time due to exposure to molecules that become adsorbed on the surface [1]. Also, low vacuum conditions, hypothetically caused by other emitting materials used in the electron gun, could collide with emitted electrons, causing high-speed electron and molecule bombardment, which can damage the CNTs on the samples [2]. It can be argued that for large-area samples, there is insufficient data to determine which of the previously mentioned adverse phenomena affects the beam the most.

When comparing the two sample sizes, a few differences in their field emission behavior are noticeable. For instance, the $4 \times 4 \text{ cm}^2$ datasets exhibit low turn-on fields in the range of $1 \text{ V } \mu\text{m}^{-1}$ to $2 \text{ V } \mu\text{m}^{-1}$. In contrast, the $2 \times 2 \text{ cm}^2$ sample requires a higher turn-on field.

Moreover, it has been observed that with each consecutive ramp-up dataset ($4 \times 4 \text{ I1}$, $4 \times 4 \text{ I2}$ and $4 \times 4 \text{ I3}$) the threshold field increases slightly. This is a well-studied effect and highlights the influence of the conditioning process on the emission properties [57]. Figure 6.1a also supports this theory, as the curve for dataset $2 \times 2 \text{ B}$ is much smoother and reaches a higher current density than dataset $2 \times 2 \text{ A}$, which was obtained first.

Fowler–Nordheim analysis supports these observations. The good linear behavior with an R^2 -factor in the range of 0.94 to 0.99 confirms that all measured

currents are based on field emission. The $4 \times 4 \text{ cm}^2$ sample datasets (see [Figure 6.3a](#)) show a gentler slope, which correlates to a high field enhancement factor or a low work function [39]. In contrast, the $2 \times 2 \text{ cm}^2$ datasets exhibit a steeper slope.

The SK-plot (see [Figure 6.3b](#)) provides a simple way to visualize how the slope and intercept of each dataset correlate to the FE behavior. The data points of the large samples are clustered in the upper left and right corner. After the first ramp-up ($4 \times 4 \text{ II}$), the slope-intercept value for the subsequently taken datasets moves towards the upper left quadrant — corresponding to a smaller tip radius or a higher field enhancement effect. These differences could also signify a change in tip structure that occurs during the sweeps, due to the previously mentioned effects.

The dataset $2 \times 2 \text{ B}$ appears in the bottom left corner. This could hint at either a larger apex radius or a less effective emission area. The observations align well with the lower turn-on fields for the $4 \times 4 \text{ cm}^2$ sample datasets and the low current density performance of the $2 \times 2 \text{ B}$ dataset mentioned previously. Interestingly, the other small sample dataset performs better in terms of current density, low turn-on field and slope-intercept value. As explained before, such variations are not unusual for CNT-based emitters, as local morphology changes due to overheating and gas absorbates can strongly influence the overall emission properties in different stages of the conditioning process [57].

The values of β and r summarized in [Table 6.2](#) can only be viewed as rough estimates, as the applied formulas are typically meant for a single CNT tip and comparative studies in the literature for this specific pattern are difficult to find. However, it is notable that the very low field enhancement factor does align with the overall mediocre FE performance. Furthermore, the calculated tip radius is approximately in the range of one hexagonally shaped CNT island (with a side length of $10 \mu\text{m}$) in the honeycomb pattern. Still, this cannot be viewed as a reliable result.

Testing the long-term stability of different samples was another research objective. Measurements for a $2 \times 2 \text{ cm}^2$ (see [Figure 6.1a](#)) demonstrate that prolonged use of the VACNT honeycomb arrays at high fields is possible. The mean current density after the ramp-up process exhibits very low fluctuations — under 5%, indicating a reasonable level of stability over an extended period. This is in accordance with results showing fluctuations of under 10% over 72 hours, as reported by Giubileo et al. [57]. Furthermore, these findings align with data from Galante [9], indicating that patterned CNT samples can emit stably for over 1000 hours without burning out.

7.2.2 Electron Beam Profile CCTB2

Finally, using the prototype and a $4 \times 4 \text{ cm}^2$ sample, an electron beam spot was produced and successfully captured, as shown in [Figure 6.4](#). Since the brightness fluctuations correlate with higher current, it can be assumed that the beam is indeed originating from the VACNT sample and is caused by an unstable beam current. However, the beam is much larger than expected. The screen (with a radius of 4 cm) is fully illuminated, suggesting that the divergence might be significantly higher than anticipated. According to the simulations, the beam should be a relatively round spot with a radius of approximately 1.8 cm (see [Table 5.2](#)).

The beam does not show an uniform luminance signal. A brighter, half-moon area can be observed at the top. When changing V_M this bright area shifts slightly, indicating that the beam is not confined to the detector screen. Another hint of a magnified beam image is the presence of darker horizontal and vertical lines, likely caused by the grid stopping the electrons, resulting in lower intensity in these regions. These distortions might be due to uneven focusing or because the electron beam that is exiting the emitter region has a much higher divergence and energy spread than expected.

The next step would be to install solenoids to focus the beam more efficiently and reduce losses. Another option could be to shorten the distance between the source and the detector by moving the detector closer and removing the Einzel lenses.

Investigating how to enhance the FE properties of the sample would be another aim for further research. One focus could be to improve the CNT anchoring, as demonstrated by Liu et al., which could improve field enhancement and the stability [2]. Furthermore, another idea would be to use residual gas analysis to understand the vacuum conditions better.

Nonetheless, even with low current, the results obtained are still promising and confirm that a dual-gridded gun design based on VACNT can function. Further research on the general setup and refining the electron gun design is therefore warranted based on the insights gained so far.

8 Potential Applications in Medicine

The advances in the production, cooling and trapping of antiprotons at CERN inspire not only further fundamental research, but also innovations that benefit society. One promising application of a low-energy decelerator complex is cancer therapy.

Typical radiotherapy modalities include photon, electron and proton beams. Additionally, several other advanced options, such as carbon ions, neutrons and antiprotons, are being investigated and discussed. In comparison to photons, which deposit their energy exponentially after a short increase, charged particles exhibit a **Bragg peak**, where most of their energy is deposited at a specific depth, followed by a steep decrease [58] [59].

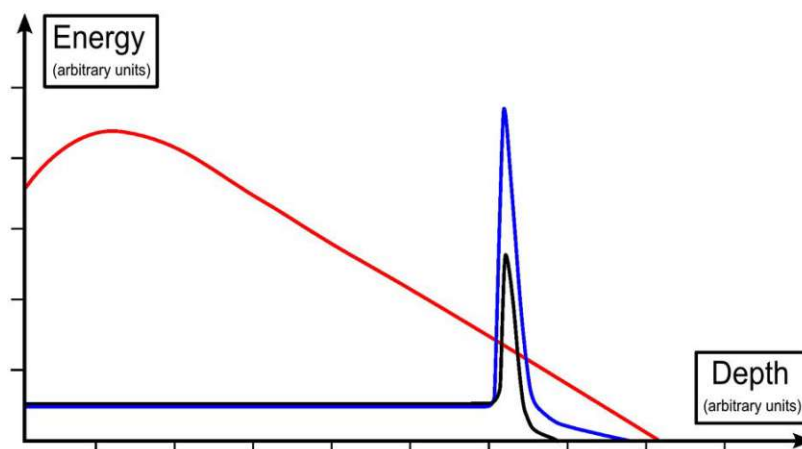


Figure 8.1: Schematic image of depth-dose profiles of a photon (red), proton (black) and antiproton beam (blue). The deposited energy is expressed relative to the plateau region. [58]

The concept of antiproton-based radiotherapy was first introduced in 1982. Studies have shown that during the entrance phase, antiprotons travel through tissue in a manner almost identical to protons [58]. However, at the end of their range, antiprotons release an additional 30 MeV of energy due to annihilation, compared to their matter counterparts. This results in practically double the deposited physical dose compared to protons. Figure 8.1 shows a depth-dose curve of photons, protons and antiprotons, clearly demonstrating the antiprotons Bragg peak that is twice as intense as that of a proton beam [60].

The extra energy deposition in the Bragg peak region presents promising outcomes, as the goal is to maximize energy delivery at a specific depth while minimizing damage to surrounding healthy tissue [60]. Comparative studies have shown that antiprotons have a 3.75 times higher ability to destroy tumorous cells due to the increased annihilation dose [61].

Another promising advantage is the possibility of real-time monitoring of the dose distribution during the irradiation process. Annihilation byproducts that are emitted can be detected using an external imaging system. Controlling beam misalignment in real time could greatly improve treatment accuracy and safety [62].

Clinical indications for treatment with antiprotons include for example re-irradiation or small tumors near critical organs where avoiding healthy tissue is especially important. Therapy-resistant volumes inside a tumor are another scenario where the high effectiveness of antiprotons can be exploited [58].

Despite these advantages, antiproton therapy has not been implemented in clinical practice. The production of antiprotons requires a highly complex and costly facility that must be maintained continuously. Currently, only the CERN accelerator complex is actively producing antiprotons, as Fermilab's Tevatron was shutdown in 2011. However, the international accelerator facility for Antiproton and Ion Research (FAIR) at GSI is under constructing, possibly allowing advanced studies and clinical trials.

Further research with more robust data is needed to determine whether antiproton radiotherapy is feasible for clinical use [58]. Enhancing electron cooling, as explored in this thesis, contributes to the production of very highly luminous beams. Reducing the size and energy spread of the antiproton beam by investigating colder beam sources for the electron cooler's electron gun is key to enabling the best initial conditions for clinical studies.

Acknowledgment

I am very grateful to my university supervisor **Michael Benedikt** for accepting me as a master's student and for his constant support during my time as a technical student at CERN.

I would like to express my deep gratitude to my supervisor **Gerard Tranquille**, for his supervision, our many discussions and the excellent guidance throughout this project. Thank you for this once-in-a-lifetime opportunity to be a part of the CERN community. I will always benefit from your immense knowledge and your valuable feedback on scientific, technical and communication competencies.

I also wish to thank my bachelor's and master's thesis co-supervisor **Karin Poljanc** – her encouragement, assistance in applications and professional and personal advice have been invaluable to my academic journey.

I would like to say many thanks, merci, danke, grazie and gracias to numerous colleagues, for their support and collaboration throughout this research:

- **James Storey**, for supporting this work and fostering a productive collaborative environment within **SY-BI-XEI**.
- **Jean Cenede**, for his contributions to designing and upgrading the prototype.
- **George Machado Jr.**, from **INL**, for his eagerness to collaborate and for producing our CNT samples.
- **Gunn Khatri, Muhammed Sameed and Volodymyr Rodin**, for their help in improving my simulation skills.
- **Wilfried Devauchelle**, for assisting me with modeling the grids.
- **Bruno Galante**, for helping me understand the project and answering all my questions.
- **Ahmed, Anite and Yasemin**, from **EN-MME-MM**, for their support with microscopy.
- **Gabriela Cabrera Castellano**, for being the best office mate and supporter.

Working at CERN has been an amazing experience, and I feel incredibly fortunate to have been part of such a dedicated and talented team at SY-BI. With their support I was able to grow on both professional and personal levels and would not like to miss this time.

Beyond CERN, I would like to take this opportunity to thank everyone who has supported my academic journey since my bachelor's degree in Technical Physics.

First, my gratitude goes to all my previous internship supervisors, who took the time to teach me the foundations of research that I still build on today: **Dihia Moussaoui** from ESRF, **Szymon Myalski** and **Claus-Stefan Schmitzer** from EBG MedAustron, as well as **Charles Sammut**, **Julian Bonello** and **Iman Farhat** from the University of Malta. In addition, I would like to mention all the amazing female physicists I met along the way, who have been a great inspiration.

I am also very grateful to **Gerhard Schütz** for his support in applications and to the dean of studies, **Eugenijus Kaniusas**, for enabling me to combine my stay at CERN with a Master's thesis.

A special note of thanks goes to my fellow students for their camaraderie and moral support over the years.

This journey would not have been the same without the unwavering support of my close friends, who stood by me through every challenge and success. A big thank you goes out to my family, who has supported me in every way possible. A very special thanks to my mother, **Angela Welker**, who not only proofread this thesis but has encouraged me to follow my passions since childhood.

Last but certainly not least, I am thankful to my partner, **Felix Höfenstock**, for being my universal constant and for believing in me – every step of the way.

Bibliography

- [1] M. T. Cole et al. “Ballasted and electrically steerable carbon nanotube field emitters.” In: *Carbon Nanotubes, Graphene, and Associated Devices V* 8462 (2012), 84620R. DOI: 10.1117/12.932388. URL: <https://doi.org/10.1117/12.932388> (cit. on pp. 1, 55).
- [2] Xinchuan Liu et al. “Enhanced field emission stability of vertically aligned carbon nanotubes through anchoring for X-ray imaging applications.” In: *Journal of Materials Chemistry C* 11 (2023), pp. 2505–2513. DOI: 10.1039/d2tc04363g. URL: <https://doi.org/10.1039/d2tc04363g> (cit. on pp. 1, 19, 55, 57).
- [3] CERN. *CERN Document Server*. 2024. URL: <https://cds.cern.ch/> (visited on 01/25/2024) (cit. on pp. 1, 3, 4, 8).
- [4] V. Chohan et al. *Extra Low ENergy Antiproton (ELENA) ring and its Transfer Lines: Design Report*. CERN Yellow Reports: Monographs. Geneva: CERN, 2014. DOI: 10.5170/CERN-2014-002. URL: <https://cds.cern.ch/record/1694484> (cit. on pp. 1, 8, 9, 11, 12).
- [5] M. Sreekanth, P. Srivastava, and S. Ghosh. “Highly enhanced field emission from copper oxide nanoparticle decorated vertically aligned carbon nanotubes: Role of interfacial electronic structure.” In: *Applied Surface Science* 508 (2020), p. 145215. ISSN: 0169-4332. DOI: <https://doi.org/10.1016/j.apsusc.2019.145215>. URL: <https://www.sciencedirect.com/science/article/pii/S0169433219340322> (cit. on pp. 1, 20, 21, 55).
- [6] G. Tranquille. *Electron Cooling*. Presentation at CERN. 2018. URL: https://indico.cern.ch/event/677170/contributions/2772417/attachments/1674327/2687473/Electron_Cooling.pdf (cit. on pp. 1, 9, 12, 23).
- [7] J. Abraham, S. Thomas, and N. Kalarikkal, eds. *Handbook of Carbon Nanotubes*. With 803 Figures and 86 Tables. Cham: Springer Nature Switzerland AG, 2022. ISBN: 978-3-030-91345-8. DOI: 10.1007/978-3-030-91346-5. URL: <https://doi.org/10.1007/978-3-030-91346-5> (cit. on pp. 1, 17, 18, 20).
- [8] D. Cai and L. Liu. “The screening effects of carbon nanotube arrays and its field emission optimum density.” In: *AIP Advances* 3 (Dec. 2013), p. 122103. DOI: 10.1063/1.4841275 (cit. on pp. 1, 18).
- [9] B. Galante. “Characterization studies of carbon nanotubes as cold electron field emitters for electron cooling applications in the Extra Low ENergy Antiproton(ELENA) ring at CERN.” Doctoral dissertation. U. Liverpool (main), 2023. DOI: 10.17638/03168931 (cit. on pp. 1, 2, 8, 9, 11, 12, 17–21, 23, 25, 30, 35, 53, 55, 56).
- [10] E. K. Anderson et al. “Observation of the effect of gravity on the motion of antimatter.” In: *Nature* 621.7980 (Sept. 2023), pp. 716–722. ISSN: 1476-4687. DOI: 10.1038/s41586-023-06527-1. URL: <https://doi.org/10.1038/s41586-023-06527-1> (cit. on p. 3).
- [11] D. Gamba et al. “ELENA Commissioning.” In: (2019), WEX03. DOI: 10.18429/JACoW-COOL2019-WEX03. URL: <https://cds.cern.ch/record/2708476> (cit. on p. 5).

- [12] M. Berz, K. Makino, and W. Wan. *An Introduction to Beam Physics*. English. CRC Press, 2015, p. 324. ISBN: 9781420011821. DOI: 10.1201/b12074 (cit. on pp. 6, 13, 14).
- [13] W. Barletta, L. Spentzouris, and E. Harms. *US Particle Accelerator School Notes*. <https://uspas.fnal.gov/materials/10MIT/Emittance.pdf>. June 2012 (cit. on pp. 6–8).
- [14] B.J. Holzer. “Introduction to Transverse Beam Dynamics.” In: (2014). Comments: contribution to the CAS - CERN Accelerator School: Course on Superconductivity for Accelerators, Erice, Italy, 24 Apr - 4 May 2013, edited by R. Bailey, CERN-2014-005, pp. 27–45. DOI: 10.5170/CERN-2013-007.27. arXiv: 1404.0923. URL: <http://cds.cern.ch/record/1693320> (cit. on p. 6).
- [15] B. Veglia. “Low energy beam dynamics simulations for ELENA optimization.” Doctoral dissertation. U. Liverpool (main), Liverpool U., 2022 (cit. on pp. 6, 8–11).
- [16] COMSOL. *Phase Space Distributions and Emittance in 2D Charged Particle Beams*. Sept. 2016. URL: <https://www.comsol.com/blogs/phase-space-distributions-and-emittance-in-2d-charged-particle-beams/> (cit. on pp. 7, 8).
- [17] COMSOL Multiphysics. *Particle Tracing Module User’s Guide, AC/DC Module*. Accessed: 2023-11-05. 2023. URL: https://doc.comsol.com/6.0/doc/com.comsol.help.particle/particle_ug_acdc.07.17.html (cit. on pp. 7, 37).
- [18] H. Poth. “Electron cooling: Theory, experiment, application.” In: *Physics Reports* 196.3 (1990), pp. 135–297. ISSN: 0370-1573. DOI: [https://doi.org/10.1016/0370-1573\(90\)90040-9](https://doi.org/10.1016/0370-1573(90)90040-9). URL: <https://www.sciencedirect.com/science/article/pii/0370157390900409> (cit. on pp. 8, 9, 11, 12, 14, 22, 23).
- [19] G.I. Budker. “An effective method of damping particle oscillations in proton and antiproton storage rings.” In: *Soviet Atomic Energy volume* 22.No. 5 (1967), pp. 438–440 (cit. on p. 8).
- [20] CERN. *ELENA - Electron Cooler*. Presented at the Electron Cooler BI Day, June 10th, 2016. 2016 (cit. on p. 10).
- [21] S. Kasap. *Principles of Electronic Materials and Devices*. 3rd ed. USA: McGraw-Hill, Inc., 2005. ISBN: 0073104647 (cit. on p. 13).
- [22] P. W. Hawkes and E. Kasper. *Principles of Electron Optics, Volume Two: Applied Geometrical Optics*. Second. London: Academic Press, 2017 (cit. on pp. 13, 15, 22, 23).
- [23] T. I. Awan et al. “Chapter 7 - Electrons in nanostructures.” In: *Chemistry of Nanomaterials*. Ed. by T. I. Awan, A. Bashir, and A. Tehseen. Elsevier, 2020, pp. 179–206. ISBN: 978-0-12-818908-5. DOI: <https://doi.org/10.1016/B978-0-12-818908-5.00007-X>. URL: <https://www.sciencedirect.com/science/article/pii/B978012818908500007X> (cit. on pp. 13, 14, 23).

- [24] S. Parveen et al. "Fowler Nordheim theory of carbon nanotube based field emitters." In: *Physica B: Condensed Matter* 505 (2017), pp. 1–8. ISSN: 0921-4526. DOI: <https://doi.org/10.1016/j.physb.2016.10.031>. URL: <https://www.sciencedirect.com/science/article/pii/S0921452616304914> (cit. on p. 14).
- [25] R. H. Fowler and L. Nordheim. "Electron Emission in Intense Electric Fields." In: *Proceedings of the Royal Society of London. Series A, Containing Papers of a Mathematical and Physical Character* 119.781 (1928), pp. 173–181. ISSN: 09501207. URL: <http://www.jstor.org/stable/95023> (visited on 02/19/2024) (cit. on p. 14).
- [26] R. G. Forbes. "Physics of generalized Fowler-Nordheim-type equations." In: *Journal of Vacuum Science & Technology B: Microelectronics and Nanometer Structures Processing, Measurement, and Phenomena* 26.2 (Apr. 2008), pp. 788–793. ISSN: 1071-1023. DOI: 10.1116/1.2827505. eprint: https://pubs.aip.org/avs/jvb/article-pdf/26/2/788/15747151/788_1_online.pdf. URL: <https://doi.org/10.1116/1.2827505> (cit. on pp. 14, 16).
- [27] D. Matte. "Ultrafast electron cold field emission from a tungsten nanotip by single cycle THz pulse." Doctoral dissertation. 2023 (cit. on p. 14).
- [28] E. Radauscher. "Design, Fabrication, and Characterization of Carbon Nanotube Field Emission Devices for Advanced Applications." Doctoral dissertation. Jan. 2015. DOI: 10.13140/RG.2.2.16376.85767 (cit. on pp. 14, 22).
- [29] N. Grigoryan, A. Roszkiewicz, and P. Chudzinski. "Generalizing Fowler Nordheim Tunneling Theory for an Arbitrary Power Law Barrier." In: *physica status solidi (b)* 260.6 (2023), p. 2200599. DOI: <https://doi.org/10.1002/pssb.202200599>. eprint: <https://onlinelibrary.wiley.com/doi/pdf/10.1002/pssb.202200599>. URL: <https://onlinelibrary.wiley.com/doi/abs/10.1002/pssb.202200599> (cit. on p. 15).
- [30] M. T. Cole et al. "Chapter 5 - Engineered carbon nanotube field emission devices." In: *Emerging Nanotechnologies for Manufacturing (Second Edition)*. Ed. by W. Ahmed and M. J. Jackson. Second Edition. Micro and Nano Technologies. Boston: William Andrew Publishing, 2015, pp. 125–186. ISBN: 978-0-323-28990-0. DOI: <https://doi.org/10.1016/B978-0-323-28990-0.00005-1>. URL: <https://www.sciencedirect.com/science/article/pii/B9780323289900000051> (cit. on pp. 15–18, 20).
- [31] Q. Chen et al. "Development of a High-Beam-Transparency Gridded Electron Gun Based on a Carbon Nanotube Cold Cathode." In: *IEEE Electron Device Letters* 43.4 (Apr. 2022), pp. 615–618. DOI: 10.1109/LED.2022.3158974 (cit. on p. 16).
- [32] C. Collins et al. "High Performance Field Emitters." In: *Advanced Science* 3 (Feb. 2016), p. 8. DOI: 10.1002/advs.201500318 (cit. on p. 16).
- [33] S. Iijima. "Helical microtubules of graphitic carbon." In: *Nature* 354 (Nov. 1991), p. 56 (cit. on p. 17).
- [34] L. Radushkevich and V. Lukyanovich. "About the structure of carbon formed by thermal decomposition of carbon monoxide on iron substrate." In: *J. Phys. Chem. (Moscow)* 26 (1952), pp. 88–95 (cit. on p. 17).

- [35] Alexandre Mariet. “Étude des effets du cuivrage et de l’irradiation par proton à 440 GeV sur les propriétés mécaniques de fils en nanotubes de carbone pour l’instrumentation des faisceaux de particules au CERN.” Thèse présentée et soutenue à Besançon, le 3 mai 2023. Thèse de doctorat. Besançon, France: Université de Franche-Comté, May 2023 (cit. on pp. 17, 18).
- [36] G. S. Bocharov and A. V. Eletsii. “Theory of Carbon Nanotube (CNT)-Based Electron Field Emitters.” In: *Nanomaterials* 3.3 (July 17, 2013), pp. 393–442. DOI: [10.3390/nano3030393](https://doi.org/10.3390/nano3030393) (cit. on p. 17).
- [37] B. C. Adhikari et al. “Optimization of Vertically Aligned Carbon Nanotube Beam Trajectory with the Help of Focusing Electrode in the Microchannel Plate.” In: *Scientific Reports* 13.1 (2023), p. 15630. ISSN: 2045-2322. DOI: [10.1038/s41598-023-42554-8](https://doi.org/10.1038/s41598-023-42554-8). URL: <https://doi.org/10.1038/s41598-023-42554-8> (cit. on p. 18).
- [38] Y. Gotoh et al. “Electron emission properties of Spindt-type platinum field emission arrays.” In: *Journal of Applied Physics* 95.3 (2004), pp. 1537–1541. DOI: [10.1063/1.1635995](https://doi.org/10.1063/1.1635995). URL: <https://doi.org/10.1063/1.1635995> (cit. on p. 19).
- [39] Jin-Ho Kim et al. “Effect of Crystallinity on the Field Emission Characteristics of Carbon Nanotube Grown on W-Co Bimetallic Catalyst.” In: *Nanomaterials* 14.10 (2024), p. 819. DOI: [10.3390/nano14100819](https://doi.org/10.3390/nano14100819). URL: <https://www.mdpi.com/2079-4991/14/10/819> (cit. on pp. 19, 56).
- [40] J. A. Liu et al. “Improvement of the field emission lifetime of freestanding vertically aligned carbon nanotubes by coating with a metallic protective layer.” In: *Vacuum* 214 (2023), p. 112179. ISSN: 0042-207X. DOI: <https://doi.org/10.1016/j.vacuum.2023.112179>. URL: <https://www.sciencedirect.com/science/article/pii/S0042207X23003767> (cit. on pp. 19, 21).
- [41] J. I. Sohn et al. “Patterned selective growth of carbon nanotubes and large field emission from vertically well-aligned carbon nanotube field emitter arrays.” In: *Applied Physics Letters - APPL PHYS LETT* 78 (Feb. 2001). DOI: [10.1063/1.1335846](https://doi.org/10.1063/1.1335846) (cit. on p. 19).
- [42] S. Neupane et al. “Synthesis and field emission properties of vertically aligned carbon nanotube arrays on copper.” In: *Carbon* 50.7 (2012), pp. 2641–2650. ISSN: 0008-6223. DOI: <https://doi.org/10.1016/j.carbon.2012.02.024>. URL: <https://www.sciencedirect.com/science/article/pii/S0008622312001455> (cit. on pp. 20, 21).
- [43] W. Huang et al. “Field emission enhancement from directly grown N-doped carbon nanotubes on stainless steel substrates.” In: *Vacuum* 198 (2022), p. 110900. ISSN: 0042-207X. DOI: <https://doi.org/10.1016/j.vacuum.2022.110900>. URL: <https://www.sciencedirect.com/science/article/pii/S0042207X22000343> (cit. on p. 20).
- [44] D. B. Williams and C. B. Carter. *Transmission Electron Microscopy: A Textbook for Materials Science*. Latest edition. Berlin, Germany: Springer, 2009. ISBN: 978-0-387-76501-3. URL: <https://link.springer.com/book/10.1007/978-0-387-76501-3> (cit. on p. 20).

- [45] G. Tripathi et al. "Erratum: "Spatial dependence of the temperature profile along a carbon nanotube during thermal-field emission" [J. Appl. Phys., 128, 025107 (2020)]." In: *Journal of Applied Physics* 131 (Apr. 2022), p. 169901. DOI: 10.1063/5.0094993 (cit. on p. 21).
- [46] Corning Incorporated. *MACOR® Machinable Glass Ceramic*. <https://www.corning.com/worldwide/en/innovation/materials-science/innovative-materials/ceramics/macor.html>. Accessed: 2024-08-07. 2024. URL: <https://www.corning.com/worldwide/en/innovation/materials-science/innovative-materials/ceramics/macor.html> (cit. on p. 25).
- [47] Direct Plastics. *PEEK Data Sheet*. Accessed: 2024-12-14. 2024. URL: <https://www.directplastics.co.uk/pdf/datasheets/PEEK%20Data%20Sheet.pdf> (cit. on p. 26).
- [48] DuPont. *Vespel High Performance Polyimide*. Accessed: 2024-12-14. 2024. URL: <https://www.dupont.com/vespel.html> (cit. on p. 27).
- [49] H. Liebl. *Applied Charged Particle Optics*. Heidelberg, Germany: Springer-Verlag, Jan. 2008. ISBN: 978-3-540-71924-3 (cit. on p. 28).
- [50] V. Rodin. "Low-energy beam preparation for the next generation antimatter experiments." Author Accepted Manuscript. Thesis. University of Liverpool, 2023. DOI: 10.17638/03177706. URL: <https://livrepository.liverpool.ac.uk/id/eprint/3177706> (cit. on p. 28).
- [51] International Iberian Nanotechnology Laboratory. *2D Materials and Devices Research Group*. <https://www.inl.int/research-groups/2d-materials-and-devices/>. Accessed: 16-Aug-2024 (cit. on p. 28).
- [52] Exosens. *Ion Beam Profiler Datasheet*. Accessed: 2024-12-13. 2019. URL: <https://www.exosens.com/system/files/2019-03/Ion-Beam-Profiler-Datasheet.pdf> (cit. on p. 30).
- [53] Mineral Processing Mica. *Mica - Properties and Uses*. Accessed: December 15, 2024. 2024. URL: <https://mpmica.com/mica/> (cit. on p. 30).
- [54] COMSOL Multiphysics. *COMSOL Multiphysics*. 2023. URL: <https://www.comsol.com/comsol-multiphysics> (cit. on p. 33).
- [55] Dassault Système Simula. *CST Studio Suite 3D EM Simulation and Analysis Software website*. 2023. URL: <https://www.3ds.com/products-services/simulia/products/cst-studio-suite/> (visited on 04/25/2023) (cit. on p. 33).
- [56] COMSOL Multiphysics. *Einzel Lens*. Accessed: 2023-11-06. 2023. URL: <https://www.comsol.de/model/einzel-lens-14405> (cit. on p. 36).
- [57] F. Giubileo et al. "Local field emission stability of vertically aligned multiwalled carbon nanotubes." In: *arXiv preprint* (2008). arXiv: 0802.4392 [cond-mat.mtrl-sci] (cit. on pp. 55, 56).
- [58] Martin-Immanuel Bittner et al. "A systematic review of antiproton radiotherapy." In: *Frontiers in Physics* 1 (Jan. 2014), p. 37. DOI: 10.3389/fphy.2013.00037. URL: <https://www.frontiersin.org/articles/10.3389/fphy.2013.00037/full> (cit. on pp. 59, 60).
- [59] Georgi Smirnov et al. "Antiproton cell experiment (ACE) at CERN's antiproton decelerator (AD)." In: *Hyperfine Interactions* 212 (2012), pp. 185–191. DOI: 10.1007/s10751-012-0638-z (cit. on p. 59).

- [60] Niels Bassler et al. “Antiproton radiotherapy.” In: *Radiotherapy and Oncology* 86.1 (Jan. 2008), pp. 14–19. DOI: 10.1016/j.radonc.2007.11.028. URL: <https://pubmed.ncbi.nlm.nih.gov/18158194/> (cit. on p. 59).
- [61] Michael H. Holzscheiter et al. “The biological effectiveness of antiproton irradiation.” In: *Radiotherapy and Oncology* 81.3 (2006), pp. 233–242 (cit. on p. 59).
- [62] Stefan Sellner, Raphael Boll, Michael Diermaier, et al. “The antiproton cell experiment—do antiprotons offer advantages over other particle beam modalities?” In: *Hyperfine Interactions* 213 (2012), pp. 127–134 (cit. on p. 59).